Ultrastructure and morphometric analysis of hippocampal synapses in the *Fmr1*$^{-/y}$ mouse model of fragile X syndrome

by

Samuel Weiser Novak
BSc. University of Guelph, 2011

A Thesis Submitted in Partial Fulfillment
of the Requirements for the Degree of

MASTERS OF SCIENCE

in the Division of Medical Sciences

Supervisory Committee

Ultrastructure and morphometric analysis of hippocampal synapses in the *Fmr1*$^{-/y}$ mouse model of fragile X syndrome

by

Samuel Weiser Novak
BSc. University of Guelph, 2011

Supervisory Committee

Dr. Patrick C. Nahirney, Division of Medical Sciences
Supervisor

Dr. Craig E. Brown, Division of Medical Sciences
Division Member

Dr. Brian R. Christie, Division of Medical Sciences
Division Member

Abstract

Supervisory Committee
Dr. Patrick C. Nahirney, Division of Medical Sciences
Supervisor
Dr. Brian R. Christie, Division of Medical Sciences
Division Member
Dr. Craig E. Brown, Division of Medical Sciences
Division Member

Fragile X Syndrome (FXS) is a prevalent monogenic disease, often presenting with cognitive and neurological disorders including autism and epilepsy. The *Fmr1* gene - transcriptionally silenced in FXS - normally encodes the Fragile X Mental Retardation Protein (FMRP), which acts as an activity dependent translational regulator at the base of dendritic spines. In an attempt to understand its role, dendritic spines in the dentate gyrus (DG) and *cornu ammonis* 1 (CA1) hippocampal regions of three-week old *Fmr1*- mice were analyzed and compared to wildtype (WT) littermate controls using electron microscopy. Dendritic spines with a continuous profile of the parent dendrite, spine neck, and spine head complete with synaptic components (presynaptic vesicles and postsynaptic densities) were included in our morphological analyses. We observed no changes in postsynaptic density length (DG: 5.69±0.30/6.18±0.85; SR: 7.55±0.87/6,96±0.33 µm/100µm^2; p=0.627/0.620), synapse density (DG: 32.3±3.8/30.3±1.9; SR: 34.4±1.8/30.7±0.5 synapses/100µm^2; p=0.655/0.270), spine head diameters (DG: 0.524±0.016/0.529±0.014; SR: 0.524±0.014/0.515±0.014 µm; p=0.098/0.20) or spine neck lengths (DG: 0.457±0.016/0.485±0.019; SR: 0.421 ± 0.015/0.425±0.017 µm; p=0.14/0.26), but found that in the DG spine necks were significantly narrower in the *Fmr1*- mice (0.193±0.0062/0.167±0.0064 µm; p=0.0002), whereas there were no changes in CA1 spine neck widths (0.162±0.0049/ 0.161±0.0061 µm; p=0.073). Estimated resistance calculated from spine necks morphologies revealed a ~1.7 fold increase in the *Fmr1*- DG compared to WT DG. These findings support that FMRP plays a role in granule cell spine neck structure and may influence synaptic signal compartmentalization and propagation in a regionally dependent manner.

Table of Contents

Supervisory Committee ii
Abstract iii
Table of Contents iv
List of Tables vi
List of Figures vii
Dedication viii
Introduction 1
1.1 Dendritic spines and the synapse 2
1.2 Fragile X syndrome 10
1.3 Dendritic spines in fragile X syndrome 13
1.4 Technical considerations 15
1.5 Rationale 15
Materials and Methods 16
2.1 Animal care 16
2.2 Genotyping 16
2.2.1 DNA extraction and purification 16
2.2.2 Polymerase chain reaction amplification of *Fmr1* 17
2.3 Processing and imaging for transmission electron microscopy 18
2.3.1 Perfusion and microdissection 18
2.3.2 Processing for transmission electron microscopy 18
2.3.3 Transmission electron micrograph acquisition 19
2.3.4 Serial section electron microscopy 21
2.4 Analysis 24
2.4.1 Synapse and spine criteria 24
2.4.2 Synapse density and post-synaptic density lengths 27
2.4.3 Dendritic spine morphometric analyses 28
2.4.4 Estimating the resistance of the spine neck 29
2.4.5 Statistical analyses 29
Results 30
3.1 Overview 30
3.2 Synapse densities and PSD lengths are not different between WT and *Fmr1*- mice 30
3.3 Quantitative analysis of spine morphological parameters 30
3.4 WT DG MML spine necks are wider than CA1 SR spine necks 34
3.5 Spine necks are narrower in the DG MML but not the CA1 SR of *Fmr1*- mice 34
3.6 Spine neck resistance is greater in the DG MML of *Fmr1*- mice 36
Discussion 45
4.1 Reliable estimates of spine morphologies from two-dimensional profiles 45
4.2 Reliable estimates of neck resistance from two-dimensional profiles 46
4.3 Functional impact of reduced neck widths 47
4.4 Limitations 48
4.5 Future Directions 48
4.6 Conclusions 49

Bibliography 50
Appendix A: *Fmr1* 62
Appendix B: CA1 SR spine morphologies 63
Appendix C: DG MML spine morphologies 64
Appendix D: Spine morphology scatterplots 65

List of Tables

Table 1: Summary table of measured synapse densities and PSD lengths from the neuropil of DG and SR subfields in WT and *Fmr1*- P21 mice. 30
Table 2: Summary table of morphological data of dendritic spines collected from the neuropil of DG and SR subfields in WT and *Fmr1*- P21 mice. 32

List of Figures

Figure 1: Overview of synaptic ultrastructure 3
Figure 2: Schematic representations of spine morphological classifications 5
Figure 3: Ultrastructure of a prototypical dendritic spine 8
Figure 4: Wiring diagram of current passing through a dendritic spine 9
Figure 5: Vibratome section of the hippocampal region in a WT P21 mouse..... 20
Figure 6: Resin-embedded 1-µm-thick toluidine-stained sections of the DG from wild-type (WT) and *Fmr1*- male P21 mice. 21
Figure 7: Resin-embedded 1 µm thick toluidine stained sections of CA1 subfield from WT and *Fmr1*- male P21 mice..... 24
Figure 8: Ultrastructure of DG granular neurons. 24
Figure 9: Ultrastructure of CA1 pyramidal neurons 27
Figure 10: ssTEM of a dendritic spine from the DG MML of a WT P21 mouse..... 28
Figure 11: Quantification of synapse density and PSD lengths..... 34
Figure 12: Spines present wide variation in their morphologies 35
Figure 13: Comparison of DG MML and CA1 SR spine morphometrics. 38
Figure 14: Morphometric analysis of dendritic spines from the DG MML. 39
Figure 15: Morphological analysis of dendritic spines from the CA1 SR. 42
Figure 16: Estimated resistances of dendritic spine necks in the DG MML 43
Figure 17: Estimated resistances of dendritic spine necks in the CA1 SR. 44
Figure 18: Cytogenetic location of *Fmr1*. 63
Figure 20: Dendritic spine morphologies from the DG MML. 64
Figure 21: Comparison of spine neck widths and neck lengths - 65
Figure 22: Comparison of spine head widths and neck lengths..... 66
Figure 23: Comparison of spine neck widths and neck lengths..... 67

Dedication

I would like to thank Dr. Nahirney for providing me with the opportunity to learn how to use the transmission electron microscope. It has been mind opening and I will forever be satisfied to wonder at the microcosms and complexity that lie just beyond the scope of my given resolution whenever I consider life.

I would also like to take this opportunity to honour my dear friend Barry, who always encouraged me in my work and play. We found a wonderful balance and I will always treasure the time we shared together.

To Ariel, thank you for being yourself and being close to me. You are a great brother and spirit and I love you.

Thanks Mom and Dad and Joan and Bubby and Dedo for always supporting me.

Introduction

Dendritic spines are specialized subcellular protrusions that emanate from dendrites of most neurons in the mammalian brain. Spines receive and transduce excitatory synaptic inputs to their parent dendrites and exhibit remarkable plasticity in their structures and functions according to their histories of activity (De Roo et al., 2008). Their coordinated plasticity is thought to facilitate cognitive and behavioural phenomena including learning and memory (Sorra and Harris, 2000). Dysfunctions in the turnover, plasticity and morphologies of dendritic spines can all manifest as neuronal dysfunction.

Neurodevelopmental disorders have far reaching consequences on the quality of life for individuals, families and society. Despite their prevalence and consequences, the pathological mechanisms underlying these disorders remain elusive and incomplete, leaving clinicians and caregivers with treatment strategies aimed at symptoms rather than the root causes of disease. Fragile X Syndrome (FXS) is the most common heritable neurodevelopmental disorder, affecting 1:4000-1:7000 men and 1:8000-1:11000 women (Song et al., 2003; Hunter et al., 2014). In FXS, the *Fmr1* gene is transcriptionally silenced causing the loss of the fragile X mental retardation protein (FMRP), an RNA-binding regulatory protein involved in the transport, stability and translation of RNA and ultimately in the development and plasticity of neurons and spine synapses (Bassell and Warren 2000; De Rubeis and Bagni 2010). The absence of FMRP manifests with often profound behavioural and intellectual disorders in humans (Hagerman et al. 2010) that have been recapitulated in a mouse model of FXS (Dutch-Belgian Consortium, 1994).

The absence of FMRP affects local activity dependent synaptic protein translation by FMRP-bound mRNA-polyribosome granules (Dictenberg et al. 2008). The synaptic disruption manifests with a salient structural phenotype in both human and mouse brains lacking FMRP: abnormal dendritic spines. However, dendritic spines are difficult to resolve adequately with diffraction-limited light microscopy and the reported differences between wild-type and *Fmr1*- spines are subtle and specific to different regions and developmental periods. This thesis the fine details of synapses and spines found on the dendritic arbours of principal neurons in the hippocampus of *Fmr1*- mice using transmission electron microscopy.

1.1 Dendritic spines and the synapse

Dendritic spines were first described over a century ago by Santiago Ramon y Cajal (Cajal 1891), the pre-eminent Spanish neuroanatomist whose camera lucida and freehand representations of sparsely labelled Golgi impregnated neurons have informed and inspired generations of neuroscientists. His foundational structural studies revealed the ubiquity of the whorling protrusions emanating from dendrites and began to describe the heterogeneity of their distributions and morphologies. Cajal proposed that dendritic spines are the loci of the synapse – connections between discontinuous neurons – and precociously suggested their role as the structural substrate for neuronal plasticity, the phenomena that facilitate the adaptive processes of the brain that include learning and memory (Cajal 1893). These suggestions stood in stark contrast to the continuous neural syncytium theory of Gerlach (Gerlach 1872) and caused a schism in the scientific community, eg. neuron theory (Retzius 1891, Berkley 1895, Schaffer 1892) and syncytium theory (Dogiel 1896, Kolliker 1896). However, the techniques of Cajal and his contemporaries were too limited in their resolution to confirm the true structures of the synapse and the dendritic spine.

Beginning in the 1950's, transmission electron microscopy (TEM) of brain tissues revealed the fine structures of neurons and synapses (Palade 1954, Palay 1955, Palay 1956, Palay 1957, Gray 1959, Gray 1959) and confirmed that chemical synapses are discontinuous (Palay 1956). Synapses are characterized by the presence of three structures: a pre-synaptic terminal or bouton with neurotransmitter concentrated in vesicles; a post-synaptic density (PSD) that acts as a scaffold for proteins including transmembrane receptor proteins; and a synaptic cleft separating the two opposing plasma membranes (figure 1) (Gray 1959, Gray 1959).

In his landmark papers, Gray distinguished between two types of synapses, asymmetrical synapses (Type I) and symmetrical synapses (Type II), according to the size of PSDs. Type II synapses are usually found on dendritc shafts and cell somas. These have less pronounced PSDs that appear symmetrical to their apposing pre-synaptic

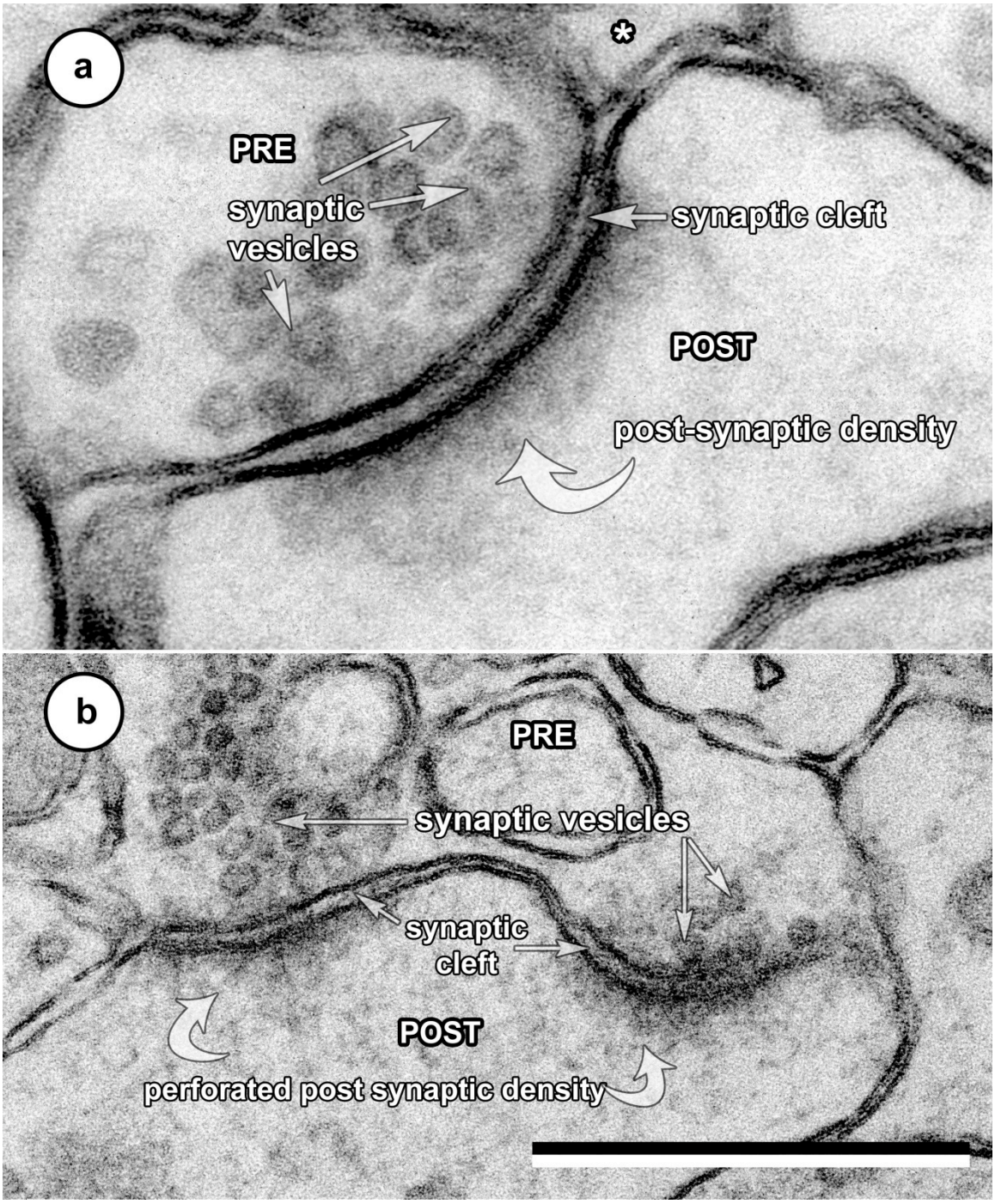

Figure 1: Overview of synaptic ultrastructure. High-resolution transmission electron micrograph (TEM) of synapses from the dentate gyrus (DG) of a post-natal day 21 (P21) wildtype mouse. (a) Synapses consist of a presynaptic terminal (PRE) containing synaptic vesicles, a synaptic cleft and a post-synaptic terminal (POST). The post-synaptic density can either be continuous as in (a) or perforated as in (b). An astrocyte (*), a type of glial cell, surrounds the pre- and post-synaptic terminals. Scale bar = 500 nm.

membrane. Type II synapses facilitate inhibitory neurotransmission and use gamma-amino butyric acid (GABA) or glycine as a neurotransmitter. They are often packed in ovoid or oblong vesicles that are typically smaller than glutamatergic vesicles. Type I synapses have thicker PSDs and therefore appear asymmetric to their pre-synaptic counterparts. These excitatory synapses use glutamate as a neurotransmitter packed in spherical vesicles about 40-60 nm in diameter and are most often found on dendritic spines.

Although they are fundamentally similar in their function, dendritic spines exhibit remarkable diversity in their morphologies (Wijetunge et al., 2014). All spines are protrusions from dendritic shafts: the distance of the synapse from the parent dendrite is measurable, thereby differentiating themselves from shaft synapses (figure 3). From foundational studies describing reconstructions of serial-sectioned cortical and hippocampal brain regions, a general system of classification by morphology emerged describing spines as mushroom, thin or stubby (Jones and Powell, 1969; Peters and Kaiserman-Abramof ,1970; Harris et al., 1992; Bourne and Harris, 2008). Mushroom spines have heads much wider than their necks; thin spines are much longer than they are wide; and stubby spines have necks about as wide as they are long (figure 2) (Harris et al., 1992). Excitatory post-synaptic sites are present as specialized regions of the membrane of the spine heads and contain a dense region termed the postsynaptic density (PSD). The head of the spine is connected to the parent dendrite by a narrow neck, thereby enabling the head to act as a relatively independent synaptic response compartment (Svoboda et al., 1996; Tonnesen et al., 2014).

In a synaptic event, glutamate is released from the presynaptic terminal into the synaptic cleft and activates specific glutamate receptors anchored in the PSD. PSDs may exist as macular or perforated plaques (figure 1b) and their size has been found to vary with the strength of the post-synaptic response (Kondo et al., 2011; Sheng and Hoogenraad, 2007). The size of the PSD is also correlated with the volume of the spine head (Peters, 1987; Spacek and Hartmann, 1983; Harris and Stevens, 1988; Harris and Stevens, 1989) the number of anchored AMPA receptors, and the ability of a spine to achieve persistent enhancement of synaptic transmission following tetanic stimulation (Kasai, et al. 2003; Cohen et al., 1977; Matsuzaki et al., 2004). In addition to the

glutamate receptors, the PSD enmeshes a heterogenous protein complex of other transmembrane receptors, secondary messenger molecules, and scaffolding proteins that connect with the filamentous actin (F-actin) cytoskeleton complex (Banker et al., 1974; Matus and Taff-Jones, 1978). Spines lack the microtubules present in dendrites and axons and are instead enriched with F-actin (Peters and Kaiserman-Abramof, 1970; Sorra and Harris, 2000) which plays an important role in spine formation, stability, motility, and elimination (Halpain, 2000; Krucker et al., 2000; Luo, 2002; Tada and Sheng, 2006; Schubert and Dotti, 2007; Ethell and Pasquale, 2005). F-actin is the substrate that underlies the dynamic morphologies of dendritic spines and is involved in the trafficking of receptors and secondary messengers to and from the PSD (Matus, 2000; Cingolani and Goda, 2008).

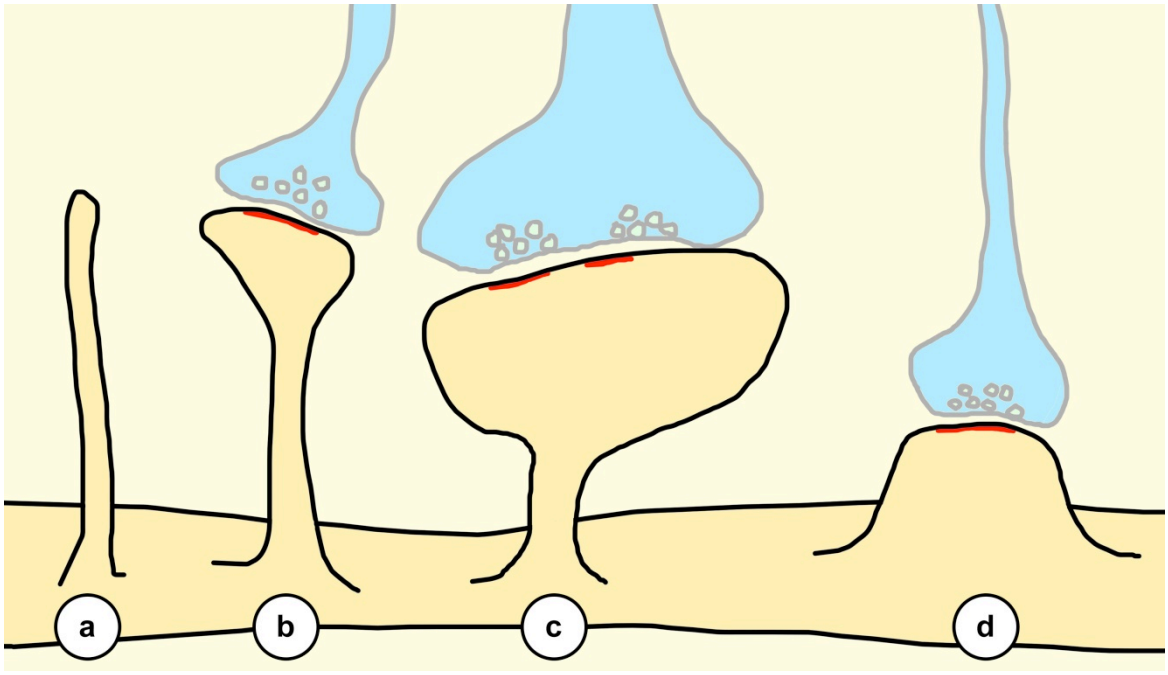

Figure 2: Schematic representations of spine morphological classifications. Spines may be roughly divided into four categories: filipodia-like spines (a) that are long with no head, thin spines (b) that are longer than they are wide; mushroom spines (c) that have heads much wider than their necks; and stubby spines (d) that have similar neck and head widths.

Some dendritic spines also contain a spine apparatus (SA). First described by Gray in his early descriptions of synapses (Gray, 1959), the SA is an elaboration of dendritic smooth endoplasmic reticulum that forms a series of sacs in the spine head and neck

(figure 3). Early studies of the SA revealed that it is present in a greater proportion of spines in adult animals relative to juvenile animals, suggesting a role in synapse maturation (Spacek, 1984; Spacek and Harris, 1997). Further studies have found a role for the SA in long-term synaptic plasticity (Deller et al., 2007), as a reservoir for glutamate receptors, and in the regulation of calcium concentrations in the spine head (Majewska et al., 2000). The absence of mitochondria, the major sink for excess intracellular calcium, in the vast majority of spine heads suggests an important role for SA in calcium regulation (Segal and Korkotian, 2014).

The proportions of spine morphologies change through development and maturation of the brain and neurons. Dendrites of immature neurons exhibit great proportions of long thin protrusions called filipodia that turnover at a high frequency (Portera-Cailliau et al., 2003). As the brain matures, the proportion of filipodia-like spines declines and the number of more stable dendritic spines with mushroom and stubby morphologies increases. In the mature brain, persistent thin spines tend to shift their morphologies towards mushroom and stubby morphologies with shorter and wider necks, indicating that these morphologies represent a more mature and persistent synaptic connection than thin spines or filipodia (Dailey and Smith, 1996; Portera-Cailliau, et al. 2003; Holtmaat and Svoboda, 2009). These mature spines are more stable and exhibit a higher sensitivity to glutamate than immature spines. They typically have larger PSDs with more complex and sometimes perforated morphologies (Popov et al., 2004) that contain a higher number of γ-amino-3-hydroxy-5-methyl-4-isoxazolepropionic acid receptors (AMPARs) and N-methyl-D-aspartate receptors (NMDARs) that are capable of generating larger excitatory post-synaptic currents (EPSCs) (Matsuzaki et al., 2001; Nicholson et al., 2006).

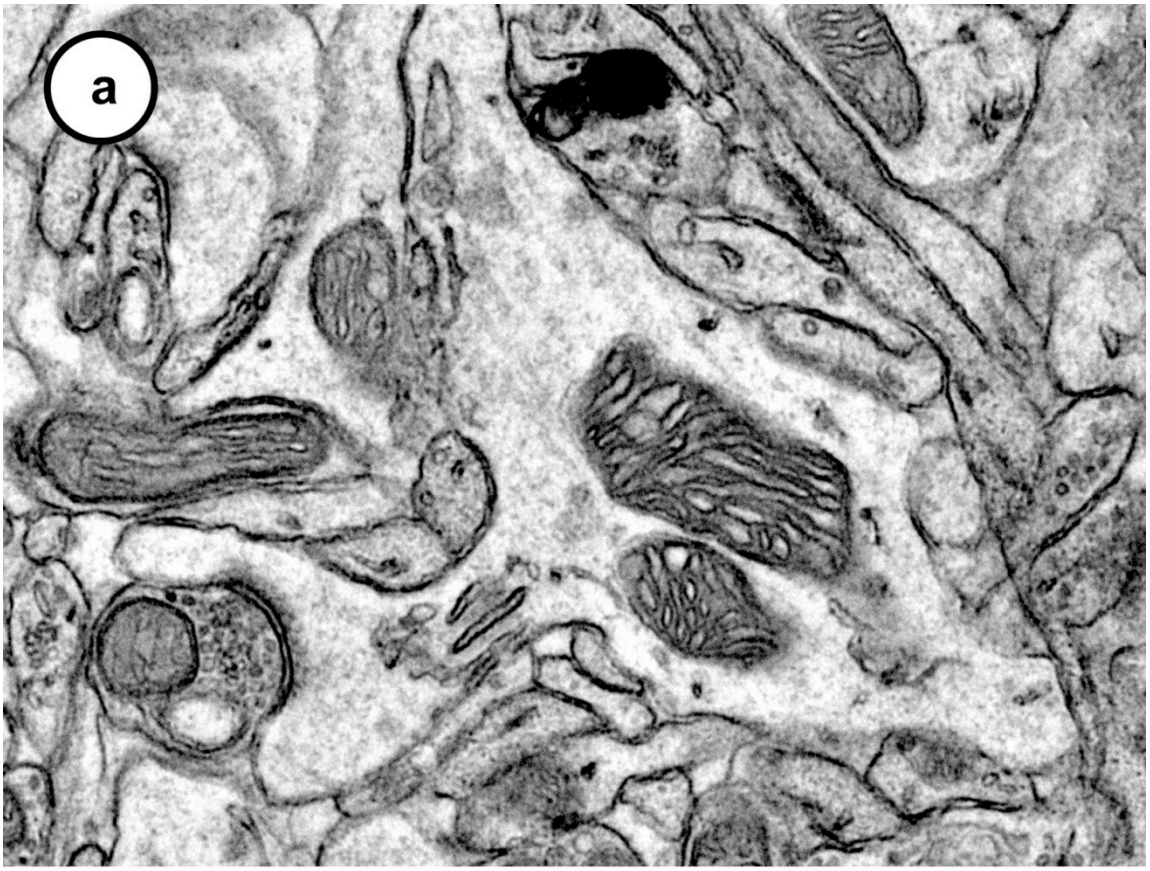
a

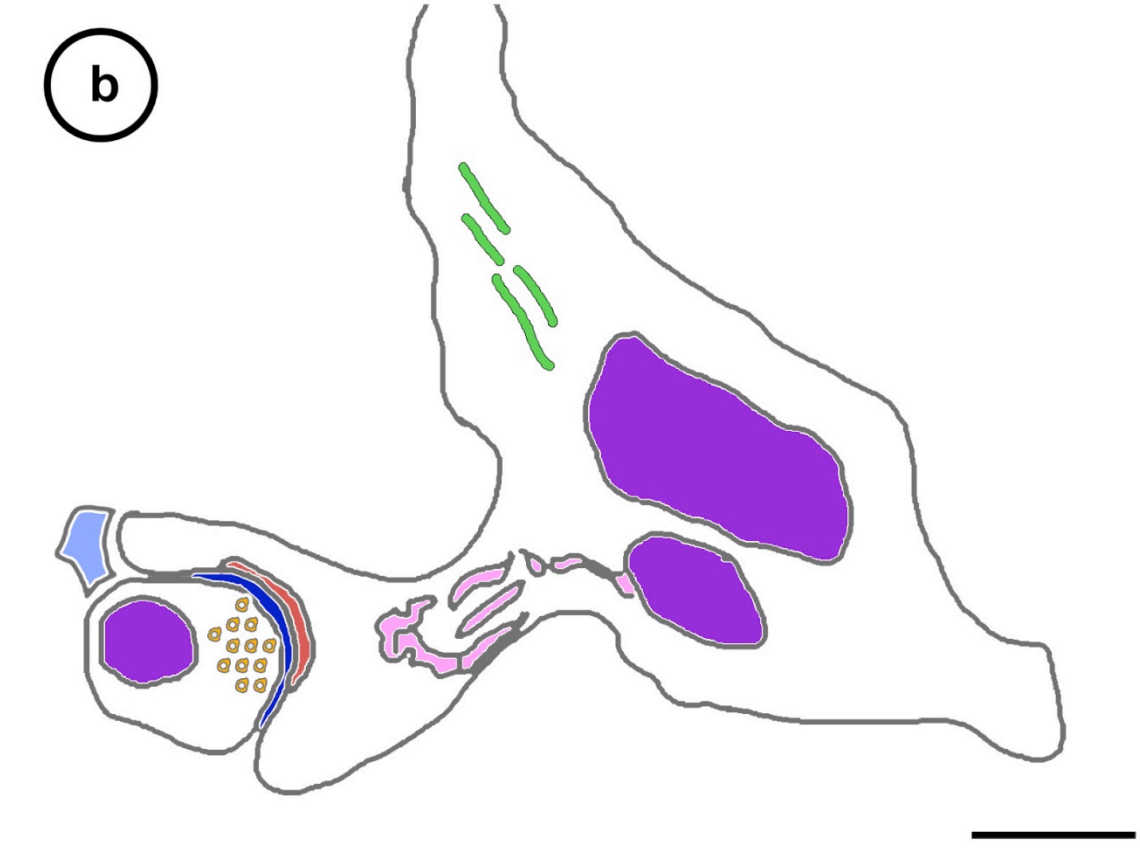
b

Figure 3: Ultrastructure of a prototypical dendritic spine. The major features of a dendritic spine are shown by TEM (a) and schematically (b). Pre- and post-synaptic mitochondria (purple), SA (pink), PSD (red), the synaptic cleft (dark blue), synaptic vesicles (orange), and an astrocyte process (pale blue) are present. Scale bar = 500 nm.

Most mature spines are very stable and may persist for months, implicating them as a physical substrate for long-term information storage (Grutzendler et al., 2002; Fu and Zuo, 2011; Kasai et al., 2010). In contrast, mature spines may still undergo structural plasticity, including head enlargement, transformation back to immature phenotypes or complete elimination (Fischer et al., 1998; Lendvai et al., 2000). This structural remodelling can be induced by long-term potentiation (LTP) and long-term depression (LTD) stimulation protocols. The induction of LTP by high-frequency stimulation causes a large calcium influx into the spine head, AMPAR insertion into the PSD, formation of new spines and enlargement of existing spines (Matsuzaki et al., 2004; De Roo et al., 2008). NMDAR and AMPAR activation upon LTP induction causes more F-actin to polymerize as spines adapt to the enhanced input (Okamoto et al., 2004). Conversely, LTD induced by low frequency stimulation triggers a very moderate calcium influx into the spine head. AMPARs are consequently withdrawn from the PSD and spines shrink or are eliminated altogether (Zhou et al., 2004; Bastrikova et al., 2008; Zhou et al., 2004; Bastrikova et al., 2008) coincident with F-actin depolymerisation (Okamoto et al., 2004).

The morphology of spines affects their abilities to compartmentalize synaptic signals. Narrow and long spine necks associated with immature spine morphologies provide a high neck resistance (R_{neck}) to the flow of molecules and current from the spine head to the dendritic compartment (figure 4). Biochemical compartmentalization of synaptic molecules (e.g. calcium and receptors, including AMPARs and NMDARs) is enhanced by larger head volumes and is impeded with increased R_{neck}. Electrical compartmentalization of current within the spine head is very sensitive to R_{neck}, where a 50% drop in R_{neck} would drop the spine EPSP by 20%-40% without significantly changing the dendritic EPSP, affecting the probabilities of activating voltage sensitive channels within the spine head (Tonnesen et al., 2014).

The level of depolarization within the spine head is relatively independent of the diameter of its parent dendrite. However, the size of synaptic depolarization in the

dendritic compartment will vary dramatically (increasing 30 fold from trunk to distal dendrites in CA1 pyramidal neurons) due to proportional changes in the impedance in dendrites of different diameters. This effect facilitates the relative location independence of dendritic EPSPs and supports that R_{neck} does not vary according to the dendritic compartment (Harnett et al., 2012).

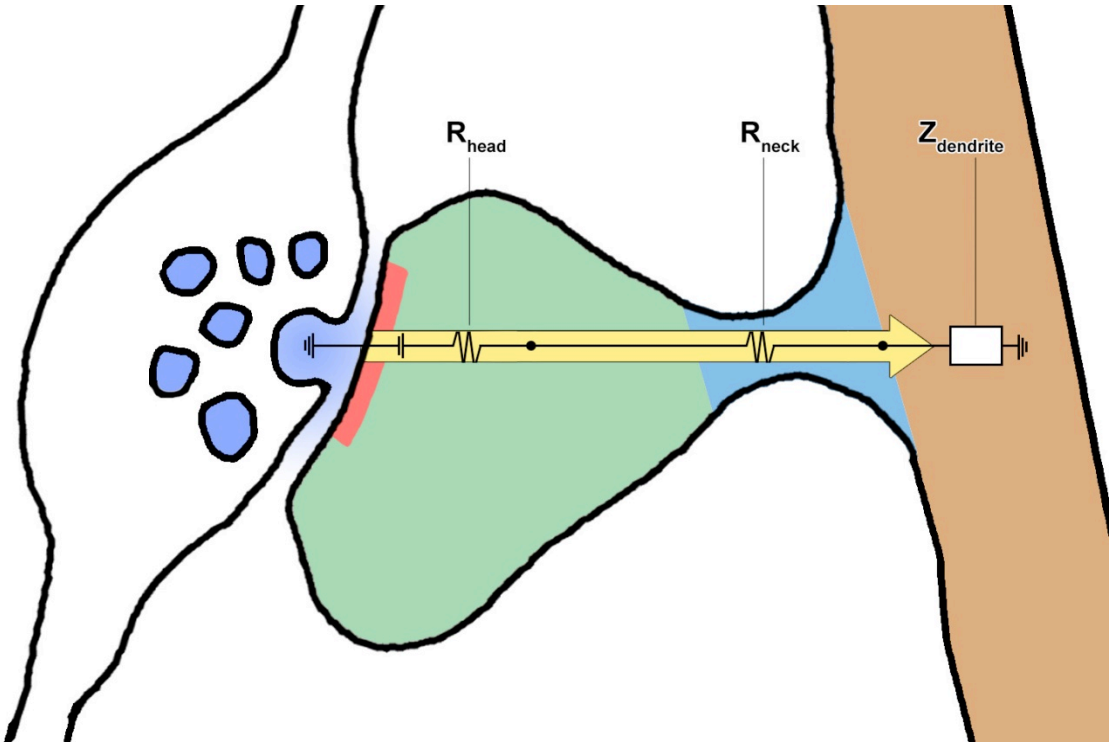

Figure 4: Wiring diagram of current passing through a dendritic spine. At excitatory synapses, glutamate (blue) is released from the pre-synaptic terminal and binds receptors anchored in the PSD (red), initiating an excitatory post-synaptic current (EPSC) (yellow). The spine head (green) provides variable resistance (R_{head}) depending on its volume and the activation states of sodium and potassium channels embedded in its membrane. The spine neck (blue) morphology determines its resistance (R_{neck}) to synaptic current and the biochemical compartmentalization of the spine head. The dendrite provides variable impedence ($Z_{dendrite}$) to the current that varies with dendritic currents (adapted from Tonnesen et al., 2014).

Since dendritic spines are responsible for most post-synaptic excitatory neurotransmission and their signals are contingent upon their morphologies, it is important to understand how changes in their morphologies affect their functions. This is especially true in the context of learning disorders, many of which have been shown to be

associated with changes at the synapse (Marin-Padilla, 1972; Purpura, 1974; Suetsugu and Mehraein, 1980; Rudelli et al., 1985).

1.2 Fragile X syndrome

Fragile X syndrome (FXS) is the most common heritable neurodevelopmental disorder (Verkerk et al., 1991), affecting 1:4000-1:7000 men and 1:8000-1:11000 women (Song et al., 2003; Hunter et al., 2014). FXS is typified by emergent intellectual disabilities, where affected children tend to encounter behavioural and cognitive difficulties as they mature. In childhood, FXS may manifest with poor motor coordination and speech pathologies (Abbeduto and Hagerman, 1997). Behavioural difficulties often emerge as hyperactivity and attention deficit disorders, repetitive behaviours like hand-flapping, poor eye contact, social phobias and anxiety (De Vries et al., 1996). Characteristic physical symptoms often manifest and include long faces, very smooth skin, large prominent ears and enlarged testes (Laing et al., 1991). FXS is associated with severe cognitive symptoms in the adult, with the average IQ of 40 in profoundly affected adult men (Lachiewicz et al., 1987; Hagerman et al., 1989; Hodapp et al., 1990).

People affected with FXS are prone to hypersensitivity to stimuli of all sensory modalities. Strong reactions to neutral stimuli can induce a condition of tactile defensiveness, a behavioural condition typified by a constitutive negative, avoidant or aversive set of responses to everyday sensations that others perceive as normal (Hagerman, 2002). The hyperarousal associated with FXS has been quantified by measuring both their electrodermal responses and their cortical responses to sensory stimuli (Musumeci et al., 1999). In electrodermal experiments, where the magnitude of conductance in the skin is used as a metric for physiological and psychological arousal, the responses of FXS affected men to stimuli of different modalities were consistently higher and demonstrated less (Miller et al., 1999). Electroencephalogram recordings of responses to somatosensory and auditory stimuli showed that FXS-affected men had greater excitability than unaffected men (Ferri et al., 1994). Furthermore, epilepsy is a common comorbidity with FXS with prevalence between 13-18% in FXS-affected men (Berry-Kravis, 2002). The etiology of FXS-associated epilepsy is not well understood; however, it can be precipitated by environmental stimuli or spontaneously arise, often as temporal lobe or partial complex seizures (Hagerman, 2002).

Before the discovery of FXS, it was well established that men were more predisposed to mental illness than women. It was in this context that FXS was first described in a pedigree analysis of a family with severely mentally disabled men, reporting that the neuropathies were inherited in an X-linked manner (Martin and Bell, 1943). Karyotyping these individuals revealed a constriction site in the long arm of the X chromosome, hence a 'fragile' X chromosome (Lubs, 1969) (see Appendix A).

Although the hereditary nature of FXS was established, researchers noticed that it had incomplete penetrance, with the severity of the phenotype amplifying through generations. Instead of the typical complete inheritance pattern, wherein no heterozygous females and all males are affected, here 20% of men were unaffected and 30% of heterozygous females were affected (Martin and Bell, 1943; Sherman et al., 1985). With advents in molecular biotechnology, the Fragile X mental retardation gene (*Fmr1*) was identified as the locus of the fragile X constriction site (Harrison et al., 1983) and a cytosine-guanine-guanine trinucleotide (CGG) repeat expansion in the 5' untranslated region of exon 1 of the *Fmr1* was identified as the specific mutation that facilitated the incomplete penetrance of disability (Fu et al., 1991; Verkerk et al., 1991). The variable number of trinucleotide repeats positively correlated with the severity of disability, providing a correlate to the incomplete penetrance phenomena observed decades earlier as premutation phenotyes (Fu et al., 1991).

The normal *Fmr1* gene has between 6-54 CCG repeats. Women are considered carriers of a premutation allele when 55-200 CCG repeats exist. Premutation alleles are associated with sex specific pathological phenotypes. Women with the permutation allele may develop fragile X associated primary ovarian insufficiency, a condition associated with ovarian failure and premature menopause (Allingham-Hawkins et al., 1999). Fragile X tremor/ataxia syndrome affects men with premutation alleles, manifesting in middle age with diverse neurological symptoms including ataxia, tremor, dementia and Parkinsonian symptoms (Greco et al., 2006). The full mutation, with greater than 200 CGG repeats, induces a critical hypermethylation of a cytosine-phosphate-guanosine (CpG) island in the promoter region of the *Fmr1* gene, resulting in complete transcriptional silencing of *Fmr1* (Colak et al., 2014) and ultimately the manifestation of FXS.

Fmr1 encodes the Fragile X Mental Retardation Protein (FMRP), the absence of which corresponds with the pathologies associated with FXS. To study the endogenous role of FMRP and the effects of its absence, a mouse model was developed by homologous recombination in embryonic stem cells to facilitate the insertion of a neomycin cassette into exon 5 of the *Fmr1* gene, effectively silencing its translation. Subsequent *Fmr1-/y* mice express virtually no FMRP, whereas their *Fmr1+/y* littermates have normal expression of both *Fmr1* transcripts and FMRP (Warren and Schalling, 1993; Dutch-Belgian Consortium, 1994). Human and mice *Fmr1* sequences are more than 95% percent homologous (Ashley et al., 1993) and have similar expression patterns in the testes and in the brain, notably both having enriched expression in the hippocampus. Furthermore, the mouse model recapitulates many behavioural and morphological correlates (discussed below) associated with the human condition (Comery et al., 1997; Eadie et al., 2012).

FMRP is thought to be involved in regulating the transport and translation of mRNAs (Bagni and Greenough, 2005). FMRP has both nuclear-export and nuclear-localization signals, facilitating travel between the nucleus and cytoplasm (Tamanini et al., 1999), and can bind 4% of human fetal brain RNA including many mRNAs encoding synaptic proteins (Ashley et al., 1993) through mRNA binding sites (Siomi et al., 1994). In addition to RNA, FMRP associates with polyribosomes (Khandjian et al., 1996; Chen et al., 2014) which collectively assemble into mRNA ribonuclear protein particles (mRNP) capable of travelling as a unit from the soma to distant targets including dendritic spines (Antar et al., 2005; Feng et al., 1997a; Feng et al., 1997b). In transport, FMRP acts as an adaptor between the anterograde transporter kinesin and mRNPs (Dictenberg et al., 2008).

However, the strongest line of evidence that accounts for abnormalities associated with FXS is the role of FMRP in the regulation of specific activity-dependent synaptic protein translation pathways. Under unstimulated conditions, FMRP acts as a translational repressor for mRNAs in the mRNP and regulates local translation at targeted locations (i.e. the synapse) in response to activity. In the absence of FMRP, FMRP-dependent regulation of the synthesis of cytoskeletal-regulating proteins (Castets et al., 2005) and scaffolding proteins is disrupted (Zalfa et al., 2007). The concentrations of PSD-

associated proteins (e.g. PSD-95) at the synapse – which are decreased in the absence of FMRP – are tightly correlated to synaptic strength and glutamate-receptor surface expression (Colledge et al., 2003), providing a mechanism for FMRP to affect synaptic strength. *Fmr1-* neurons are hypersensitive to group 1 metabotropic glutamate receptor 5 (mGluR5) signalling which leads to exaggerated mGluR5-induced LTD and consequent protein synthesis (Bear et al., 2004; Huber et al., 2002; Dölen and Bear, 2008; Osterweil et al., 2010). Normally, mGluR stimulation promotes the local synthesis of proteins that stabilize LTD as well stimulating the synthesis of FMRP (Weiler et al., 1997), which then provides negative feedback to the LTD protein synthesis cycle (Ronesi and Huber, 2008). Without FMRP, mGluR5-induced LTD and associated local protein synthesis is disinhibited and there is an overabundance of protein (Qin et al., 2005), resulting in enhanced LTD and abnormal dendritic spine morphologies (Koekkoek et al., 2005).

In humans, the gross brain morphologies of men with full-mutation FXS tend to have some abnormalities, including a smaller cerebellar vermis, enlargement of fourth and lateral ventricles, and an enlarged hippocampus (Hessl et al., 2004). However, the most salient structural phenotype consistent between *Fmr1-* humans and mice are dendritic spine abnormalities.

1.3 Dendritic spines in fragile X syndrome

Some of the first neuroanatomical findings associated with developmental neuropathologies described changes in the densities, sizes and shapes of dendritic spines (Marin-Padilla, 1972; Purpura, 1974) and there is mounting evidence that FXS pathologies originate at the synapse and dendritic spine. Abnormal dendritic spine densities have been reported extensively in both *Fmr1-* humans and mice. In human autopsy studies using Golgi staining, FXS patients had a higher spine density in the cortex than age matched controls (Irwin et al., 2001). These results have been recapitulated to some extent in animal models in developmentally and spatially distinct patterns and, particularly confounding, may be reversed by environmental enrichment (Restivo et al., 2005). Spine densities are reported to be higher on *Fmr1-* layer V cortical dendrites using Golgi staining or fluorescently-labelled fixed tissue (Comery et al., 1997; Galvez and Greenough, 2005; McKinney et al., 2005) and throughout development in the dentate gyrus (DG) in Golgi-stained tissue (Grossman et al., 2010). However, recent live

imaging studies have reported conflicting results with a near consensus that cortical spine densities are normal in *Fmr1*- mice (Pan et al., 2010; Cruz-Martín et al., 2010; Harlow et al., 2010; Meredith et al., 2007) or, alternatively, reveal a phenotype that is dependent upon development, with higher densities reported only in the first post-natal week (Nimchinsky et al., 2001). These developmental disparities suggest that an increase in cortical spine density may be due to an early period of overproduction followed by a failed period of dendritic pruning, as the increased density appears to manifest early in development (P7), disappear in adolescence (P25) (Nimchinsky et al., 2001), and return by adulthood (P75) (Galvez and Greenough, 2005). The discrepancies observed between techniques and time-points clearly highlight the need for more data and meticulous technical considerations, as perfusion conditions may dramatically affect spine densities (Park et al., 1996; Kirov et al., 2004; Popov et al., 2007; Tao-Cheng et al., 2007).

As summarized earlier, spine morphologies are integral to the function of the synapse, neuron, and brain. The first observations of abnormal spines in FXS autopsy studies reported an unexpected proportion of long tortuous spines on cortical neuron dendrites of humans (Rudelli et al., 1985; Hinton et al., 1991) and mice (Comery et al., 1997; Nimchinsky et al., 2001; Galvez and Greenough, 2005; Restivo et al., 2005; Dölen and Bear, 2008), sometimes in the absence of changes in spine density (Irwin et al., 2002; Meredith, et al. 2007). *In vivo*, cortical spines in *Fmr1*- mice present a delay in turnover and maturation from filipodia to mushroom morphologies (Cruz-Martín et al., 2010).

Although people with FXS almost always have learning and memory problems, no post-mortem studies have looked at the status of spines in the hippocampus and few studies have examined the state of spines in the hippocampus – the brain region associated with learning and memory in both humans (Lavenex and Lavenex, 2013) and mice (Pooters et al., 2015) – of *Fmr1*- mice. The most promising mechanism for learning and memory in the hippocampus are activity-dependent changes to synaptic strength and spine morphologies (Fifkova and Morales, 1989; Kasai et al., 2003; Kasai et al., 2010) both of which appear to be affected in *Fmr1*- mice (De Rubeis and Bagni, 2010). In contrast to their cortical counterparts, spines of the cornu-ammonis 1 (CA1) subregion of the hippocampus normally mature from stubby spines into longer thinner spines through development (Harris et al., 1992). Spines from CA1 neurons are longer in the *Fmr1*-

mouse at P7 (Bilousova et al., 2009) and in adult animals (Levenga et al., 2011). In another study, adult CA1 pyramidal cell dendrites have more stubby and thick spines and the WT mice have more long thin spines. In this same study, the opposite phenotype was reported in the cortex (Grossman et al., 2006). The DG presents longer, immature spines in *Fmr1*- mouse tissue throughout development (P15-P60) (Grossman et al., 2010). However, previous studies of spines morphologies in *Fmr1*- mice have all used diffraction-limited light microscopic techniques and were therefore unable to provide robust estimates of spine neck morphologies and other ultrastructural features.

1.4 Technical considerations

Few studies have used transmission electron microscopy (TEM) to investigate the properties of spines and synapses in FXS autopsy tissue (Rudelli et al., 1985) and *Fmr1*- mice (Jung et al., 2012; Jung et al., 2015) and none have used TEM to specifically investigate post-synaptic spine ultrastructure. Other studies have used fluorescent labelling and Golgi impregnation techniques limited in their resolution to a minimal resolution of 50 nm with super resolution techniques, like stimulated-emission-depletion microscopy (STED) (Wijetunge et al., 2014), and are more often closer to a resolution of 200 nm (laterally) – 400 nm (axially) (Dumitriu et al., 2011). These light microscopic techniques are, however, unable to reveal the fine structural features of the synapse. The ultrastructural characterization of dendritic spines in the *Fmr1*- mouse is a long awaited contribution to the study of FMRP function and FXS (Portera-Cailliau, 2012).

1.5 Rationale

Ultrastructural differences present in *Fmr1*- mice have been understudied, especially in the hippocampus. Many studies have described changes in the morphologies of dendritic spines using a variety of labelling techniques for light microscopic analysis. However, results are often conflicting and direct comparisons between studies are complicated by differences in the methodologies, age and brain regions examined. With the precision of electron microscopy and large sample populations of dendritic spines, the aim of this study is to describe ultrastructural features in the dendritic spines of the DG middle molecular layer (MML) and CA1 stratum radiatum (SR), and to provide a useful working model for high-throughput analysis of spine morphologies from TEM micrographs.

Materials and Methods

2.1 Animal care

All animal procedures were performed in accordance with the animal care protocols set forth by the University of Victoria Animal Care Centre and the Canadian Council on Animal Care. Animals were coded prior to genotyping and investigators were blinded prior to analyses.

Littermate male pups from breeding pairs comprised of heterozygous *Fmr1*$^{+/-}$ female and wild type male C57Bl/6 mice provided by Dr. Brian Christie (University of Victoria, Victoria, BC, Canada). Carrier female mice were originally generated by Dr. Mark Bear (Massachusetts Institute of Technology, Cambridge, MA, USA). A total of five wild type (WT) and four *Fmr1*$^{-/y}$ (*Fmr1*-) mice were used in this study.

2.2 Genotyping

To determine the integrity of *Fmr1* alleles, genotypes of the mice were determined from ear punches and tail snips collected in clean 1.5 mL Eppendorf tubes (Eppendorf, Hauppage, NY). Ear punches were collected between post-natal days 10-14 and were used for both genotyping and to code and identify animals prior to perfusion. Tail snips were collected immediately prior to perfusion on post-natal day 21. All tissues were kept at –20°C until further processing.

2.2.1 DNA extraction and purification

The Purelink Genomic DNA Purification Kit (Invitrogen, Carlsbad, CA, USA) was used for tissue digestion and DNA extraction and purification. Tissue samples were immersed in 180 µL of digestion buffer and 20 µL of Proteinase K in DNAase/RNAase free 1.5 mL Eppendorf tubes and incubated at 55°C with mixing at 300 revolutions per minute (RPM) on an Eppendorf Thermomixer (Eppendorf) overnight. Samples were either frozen and stored at -20°C or centrifuged at 15,000 RPM for 3 minutes in a microcentrifuge (ThermoIECMicromax, Fisher Scientific, Nepean, ON, Canada).

Supernatant fractions were transferred to new Eppendorf tubes with 20 µL RNAase, vortexed, and incubated for 2 minutes at room temperature. A total of 200 µL of lysis buffer was added to each tube followed by vortexing and the subsequent addition of 200

μL of 100% ethanol and a final vortex step. Lysates were transferred to new spin columns and centrifuged at 10,000 RPM for 1 minute in a microcentrifuge.

Collecting tubes were discarded and the spin columns were replaced in fresh collecting tubes. 500 μL of Wash Buffer I was added to each spin column before centrifugation under identical conditions. Collection tubes were discarded and the spin columns were replaced into fresh collecting tubes for another wash. Subsequently, 500 μL of Wash Buffer II was added to each spine column prior to centrifugation at 21,000 RPM for three minutes. Collecting tubes were discarded once again and the spin columns were replaced into fresh collection tubes. Then 100 μL of Elution Buffer was added to each column and incubated at room temperature for 1 minute. Samples were centrifuged again at 21,000 RPM for 1 minute. Collection tubes containing the sample eluate were either then stored at -20°C or processed for polymerase chain reaction (PCR) amplification of *Fmr1*.

2.2.2 Polymerase chain reaction amplification of *Fmr1*

Wildtype (WT) primers for a 456 base pair (bp) sequence and *Fmr*- KO primers for an 800 bp sequence were incorporated in the PCR mixes to differentiate between WT and *Fmr*- KO tissue samples (see Appendix A:*Fmr1*). The PCR mix consisted of: 1.25 μL (20 μM) of each forward and reverse primer; 0.5 μL (5 U/μL) of Taq DNA polymerase (Invitrogen Canada, Burlington, ON, Canada); 11 μL of nuclease-free H2O; 2.5 μL of 10X PCR reaction buffer (no $MgCl_2$, Invitrogen, Carlsbad, CA, USA); 2.5 μL (50 mM) of $MgCl_2$ (Invitrogen); 2.0 μL (2.5 mM) deoxyribonucleotide triphosphate; finally, 4 μL of sample eluate was added to the PCR mix. The solution was immediately covered with 20 μL of mineral oil to prevent evaporation.

Thermal cycling of samples was achieved with a Thermomixer R (Eppendorf). Five temperatures were held for different lengths of time: samples were heated to 94°C for five minutes, before 35 PCR cycles (60 seconds at 94°C → 90 seconds at 65°C →150 seconds at 72°C). Finally, samples were cooled to and stored at 4°C until PCR product separation by gel electrophoresis.

Wells of gel plates containing 1.5% agarose in 1X Tris- acetate-ethylenediaminetetraacetic acid buffer doped with SybrSafe DNA stain (Invitrogen, Eugene, OR, USA) were then loaded with samples. The first well was loaded with 3 μL of the 100 base pair DNA ladder (Fermentas). Subsequent wells were loaded with 9 μL

of PCR product plus 1 μL of 6X DNA loading dye (Fermentas, Burlington, ON, Canada). Samples were separated with 50 V for 75-80 minutes and DNA bands were visualized using the UV light source of a BioRad transilluminator (BioRad, Hercules, CA).

2.3 Processing and imaging for transmission electron microscopy

2.3.1 Perfusion and microdissection

Mice were deeply anaesthetized with isofluorane before transcardial perfusion. Mouse weights were recorded prior to anaesthesia. Under a dissecting microscope (Kodak) equipped with flexible fibre optic lighting, a rostral incision was made from the mouse's belly towards its throat, exposing the peritoneum. Taking care not to knick the liver, the abdominal cavity was exposed and lateral incisions were made to expose the diaphragm. An incision through the diaphragm and the right rib cage exposed the still-beating heart.

A butterfly needle (21 guage) was inserted into the left ventricle and the mouse was perfused with heperanized phosphate buffered saline (x1.5) from a gravity-fed perfusion apparatus. The right atrium was then nicked to allow free exsanguination. After the blood was cleared – approximately 3 minutes – 50-75 mL of fixative solution (1.5% paraformaldehyde and 1.5% glutaraldehyde in 0.15 M sodium cacodylate buffer) (Electron Microscopy Sciences, Hatfield, PA, USA) was administered into the mouse.

Brains were extracted, weighed, and left in the same fixative overnight before coronal thick sectioning with a vibrating microtome (Leica) set to 250 μm. Sections containing the dorsal hippocampus (-2 ± 0.5 mm Bregma) were microdissected into 1 mm^2 tissue blocks. Sections of the dentate gyrus spanned the hilar, granule cell and molecular layers of the upper blade. CA1 samples were collected from at least 100 μm lateral to the ventricles and included the stratum oriens, pyramidal cell layer, and stratum radiatum.

2.3.2 Processing for transmission electron microscopy

Samples were post-fixed with 1% osmium tetroxide containing 1% potassium ferrocyanide (reduced osmium) in sodium cacodylate buffer for 2 hours at room temperature on a rotating mixer, rinsed twice in deionized water and *en bloc* stained with aqueous 2% uranyl acetate for 2 hours. Samples were then dehydrated in ascending ethanol concentrations (2 x 50, 70, 80, 95, 2 x 100%) and infiltrated with a 1:1 mixture of 100% ethanol and Spurr's Low Viscosity resin (Electron Microscopy Sciences, Hatfield,

PA, USA) for 1 hour before transferring to pure Spurr's resin overnight on an angled rotating mixer. Samples were mixed with fresh Spurr's in the morning before embedding in BEEM capsules (BEEM Incorporated, West Chester, PA, USA).

Thick 0.5-1 μm sections were first cut with a glass knife on an ultramicrotome (UltraCut E, Reichert-Jung) and stained with 1% Toluidine blue (aq) for inspection with a light microscope (figures 2-5). Candidate samples were then trimmed with a razor blade for ultrathin sectioning. Ultrathin sections (40-70 nm) were cut with a 45˚ diamond knife (Diatome) and collected on 1 x 2 mm parlodion-coated copper slotted grids (Electron Microscopy Sciences).

2.3.3 Transmission electron micrograph acquisition

Prior to imaging samples, a replica carbon grid (Electron Microscopy Sciences) was imaged at all relevant magnifications for scale calibrations.

Regions of interest (ROIs) were imaged using a JEM-1400 transmission electron microscope (JEOL) equipped with an Orius SC1000 digital camera (Gatan). Digital Micrograph software (Gatan) equipped with automated montage functionality was used to capture panoramic views of membrane-supported sections.

An ROI was first identified at low magnification: DG ROIs were 80-120 μm from the apex of the granular cell layer (GCL) in the middle molecular layer (MML) whereas CA1 ROIs were 70-100 μm from the base of the pyramidal cell layer into the stratum radiatum (SR). An ROI was then inspected for quality at high magnification. Samples were excluded from further analysis if: a) there was overwhelming perfusion artifact (*e.g.*, massively swollen vascular glia and degenerative multilamellar bodies); or b) excessive contamination artifact of the section or membrane including folds, holes, and particulate matter that obscured the ROI.

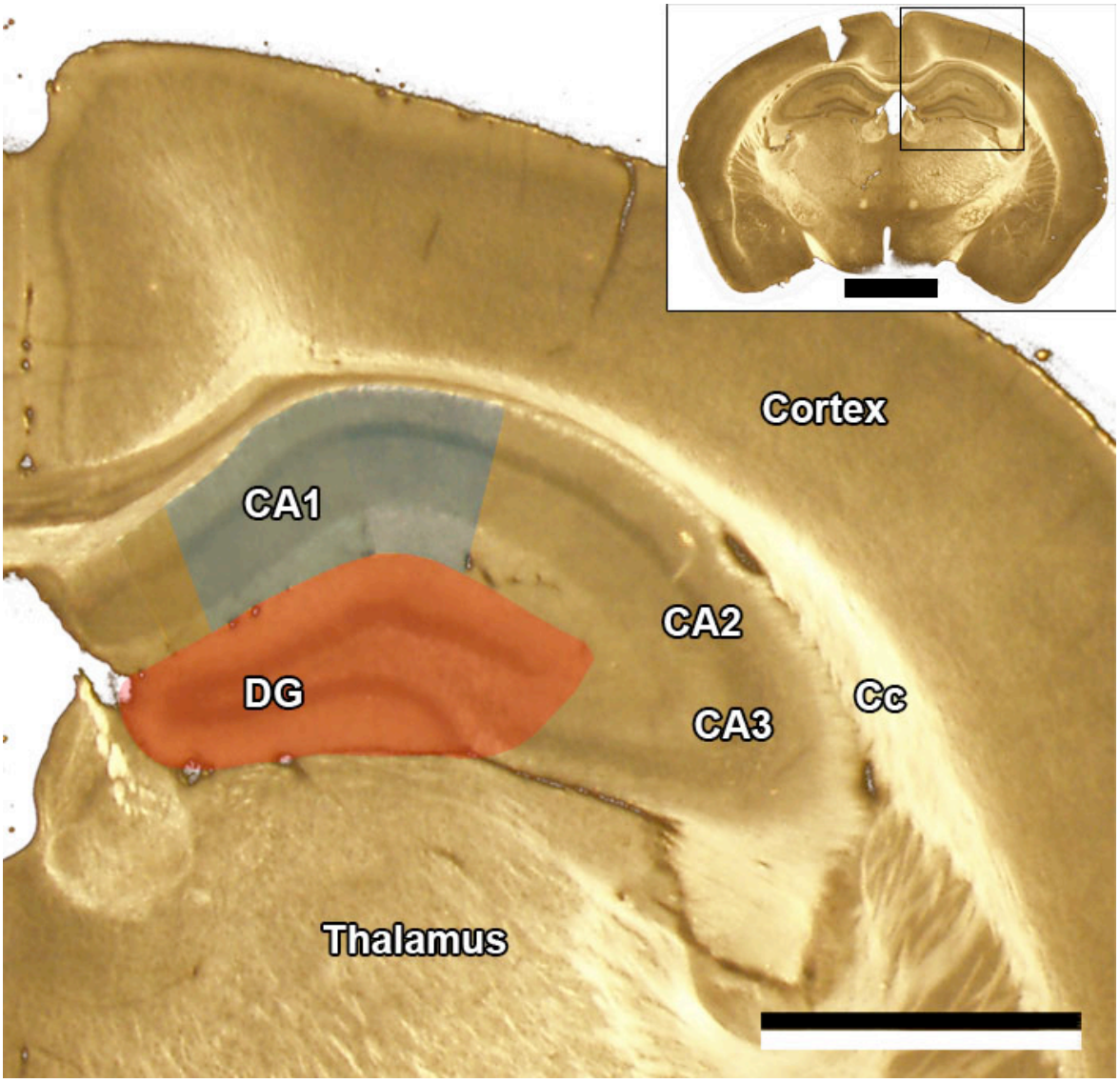

Figure 5: Vibratome section of the hippocampal region in a WT P21 mouse. Colorized boundaries indicate the microdissected regions the DG (red) and the CA1 (blue) subfields of the hippocampus used in the study. Scale bar is 1 mm. *Inset:* an overview of the section located -2 mm Bregma. Scale bar is 2mm. *Cc:* corpus collosum.

A low resolution (~20nm/pixel) montage capturing the position of the ROI relative to the cellular layers of the DG (figure 8) and CA1(figure 9) and an extensive high-resolution (≤ 3nm/pixel) montage capture of the ROI were acquired as series of tiff files. The approximately rectangular high-resolution montage was captured parallel to the orientation of the cell layer and encompassed at least 2500μm^2 of neuropil. Montages

were stitched using ptGUI software (New House Internet Services B.V., Rotterdam, The Netherlands).

2.3.4 Serial section electron microscopy

Prior to ultrathin serial sectioning, the block face was trimmed to a very short trapezoid 300 µm wide using glass blades. Ribbons of 60 nm serial sections were collected on parlodion-coated slotted grids and panoramic images of the ROI were collected as described above for each section on the membrane. Panoramas were stitched in ptGUI and roughly aligned and cropped in Photoshop (Adobe). The roughly aligned stack was then imported into the TrakEM2 extension of ImageJ (NIH). Sections were further aligned by rigid transformation algorithms. Spine heads, necks, PSDs, pre-synaptic terminals, and dendritic compartments were traced as different area lists. Three-dimensional reconstructions were rendered and smoothed and assembled as a plate in Photoshop (Adobe) (figure 10).

Next page: **Figure 6: Resin-embedded 1-µm-thick toluidine-stained sections of the DG from wild-type (WT) and *Fmr1*- male P21 mice.** The DG is divided into an upper blade (UB) and a lower blade (LB) with a central hilar region (Hi) that contains the axonal projections that stream from the dentate gyrus to the CA3 subfield. The granule cell layer (GCL) is a tightly packed layer of small neuron somata that project their apical dendrites into the molecular layer, where afferent axons from the entorhinal cortex synapse on dendritic spines of the granule cell dendrites in the middle molecular molecular layer (MML). Arrowheads indicate blood vessels. There were no obvious differences in GCL, MML, or Hi thicknesses or volumes between WT and *Fmr1*- mice. Arrowheads indicate blood vessels. Scale bar = 50 µm.

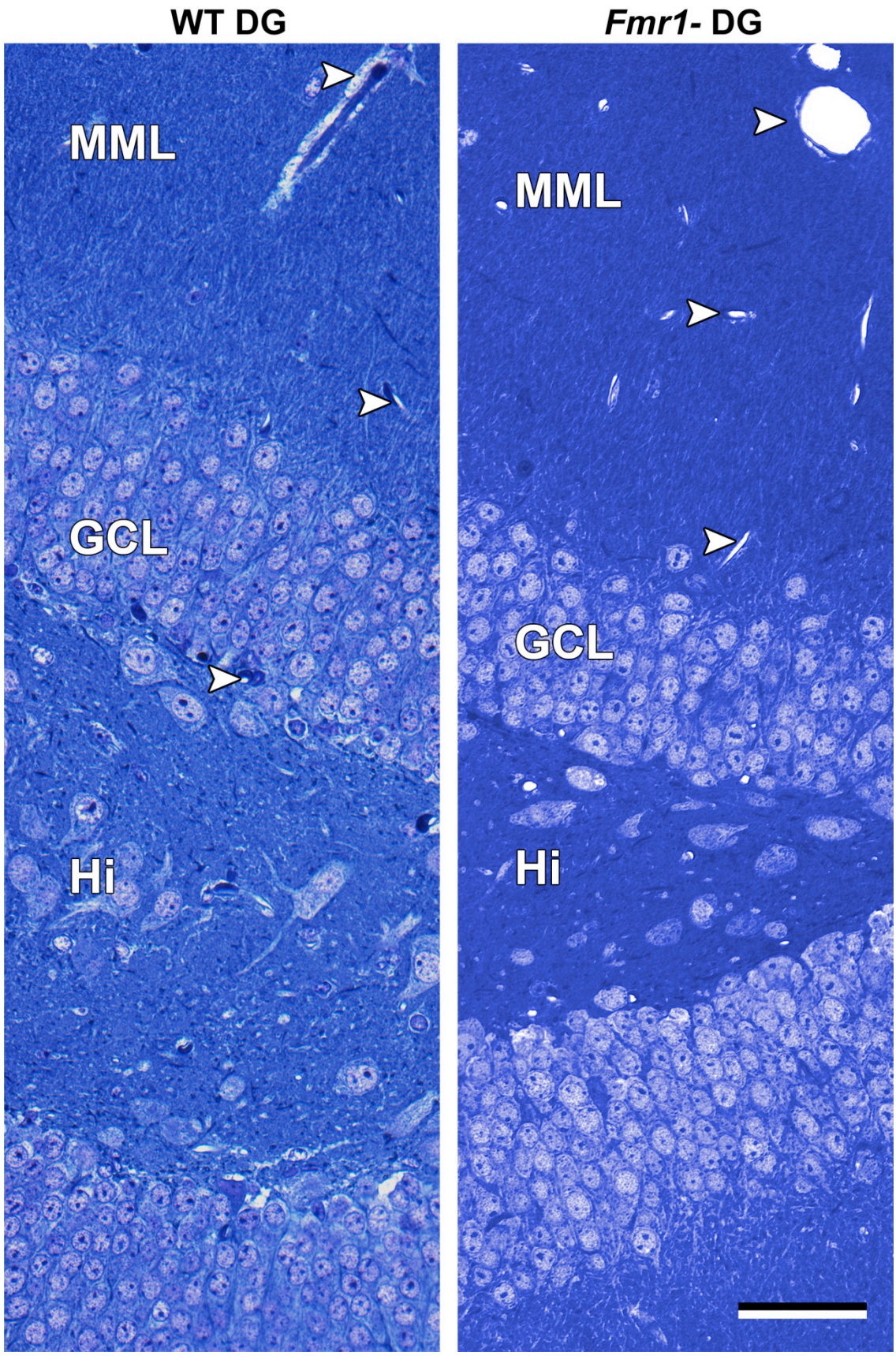
WT DG
Fmr1- DG
MML
GCL
Hi
MML
GCL
Hi

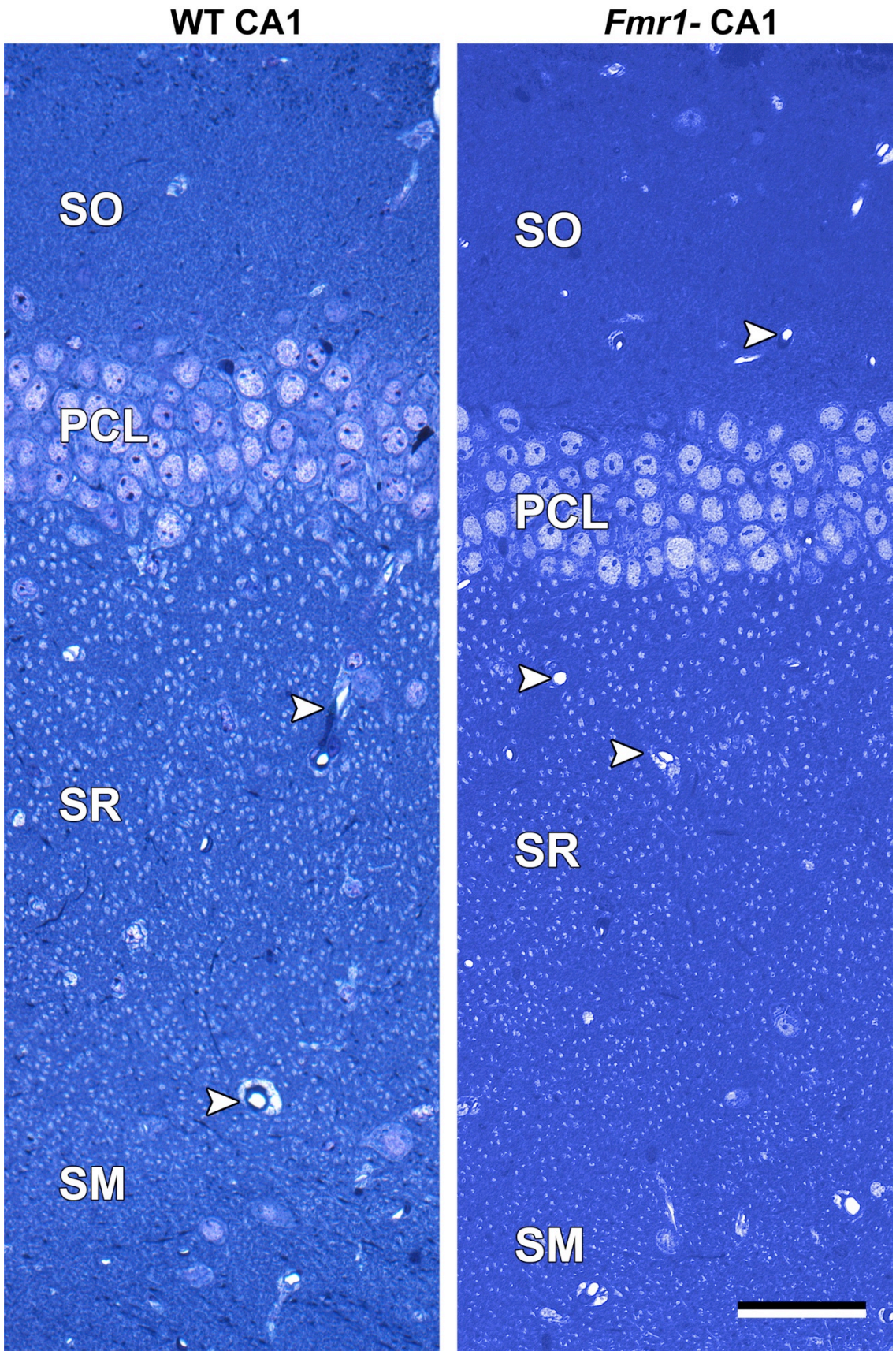
WT CA1
Fmr1- CA1
SO
PCL
SR
SM
SO
PCL
SR
SM

Figure 7: Resin-embedded 1 µm thick toluidine stained sections of CA1 subfield from WT and *Fmr1-* male P21 mice. The pyramidal cell layer (PCL) contains large cell soma of the pyramidal cell neurons. They project basal dendrites into the stratum oriens (SO) and apical dendrites into the stratum radiatum (SR) and stratum lacunosum-moleculare (SM). SO synapses receive most inputs from commissural fibers, whereas SR and SM synapses receive inputs from both the entorhinal cortex through perforant path fibers and from the Schaffer collateral (CA3→CA1) fibers. Most efferent pyramidal cell neuron axons pass through the SO to the alveus towards cortical regions through the subiculum and entorhinal cortex (Lavenex and Lavenex, 2013). Arrowheads indicate blood vessels. No obvious differences were noted in CA1 or PCL subregion thicknesses or volumes in WT and *Fmr1-* mice. Scale bar = 50 µm.

2.4 Analysis

2.4.1 Synapse and spine criteria

For both density estimates and morphological analyses, strict inclusion criteria were enforced for the selection of synapses and spines, respectively. Synapses were defined as having two compartments, one with a post-synaptic density immediately opposite to a compartment containing synaptic vesicles. Only spines that had both a synapse and a continuous profile from the parent dendrite through the spine neck to the spine head were included in morphological analyses.

Next page: **Figure 8: Ultrastructure of DG granular neurons.** TEM of granular cell somata within the GCL of the DG in a WT P21 mouse. A granular cell (shaded red) contains an apical dendrite projecting towards the molecular layer. Scale bar = 5 µm.

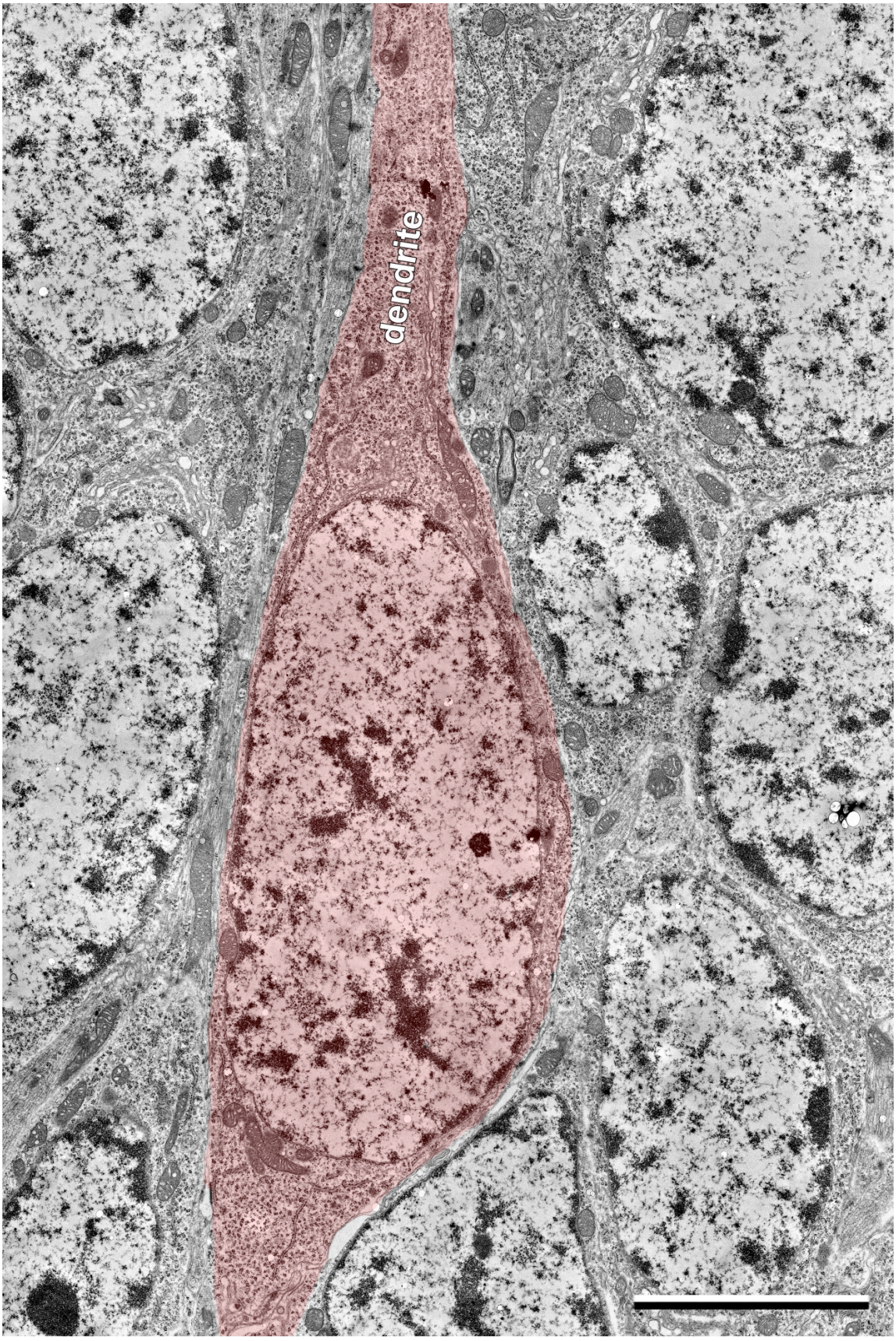
dendrite

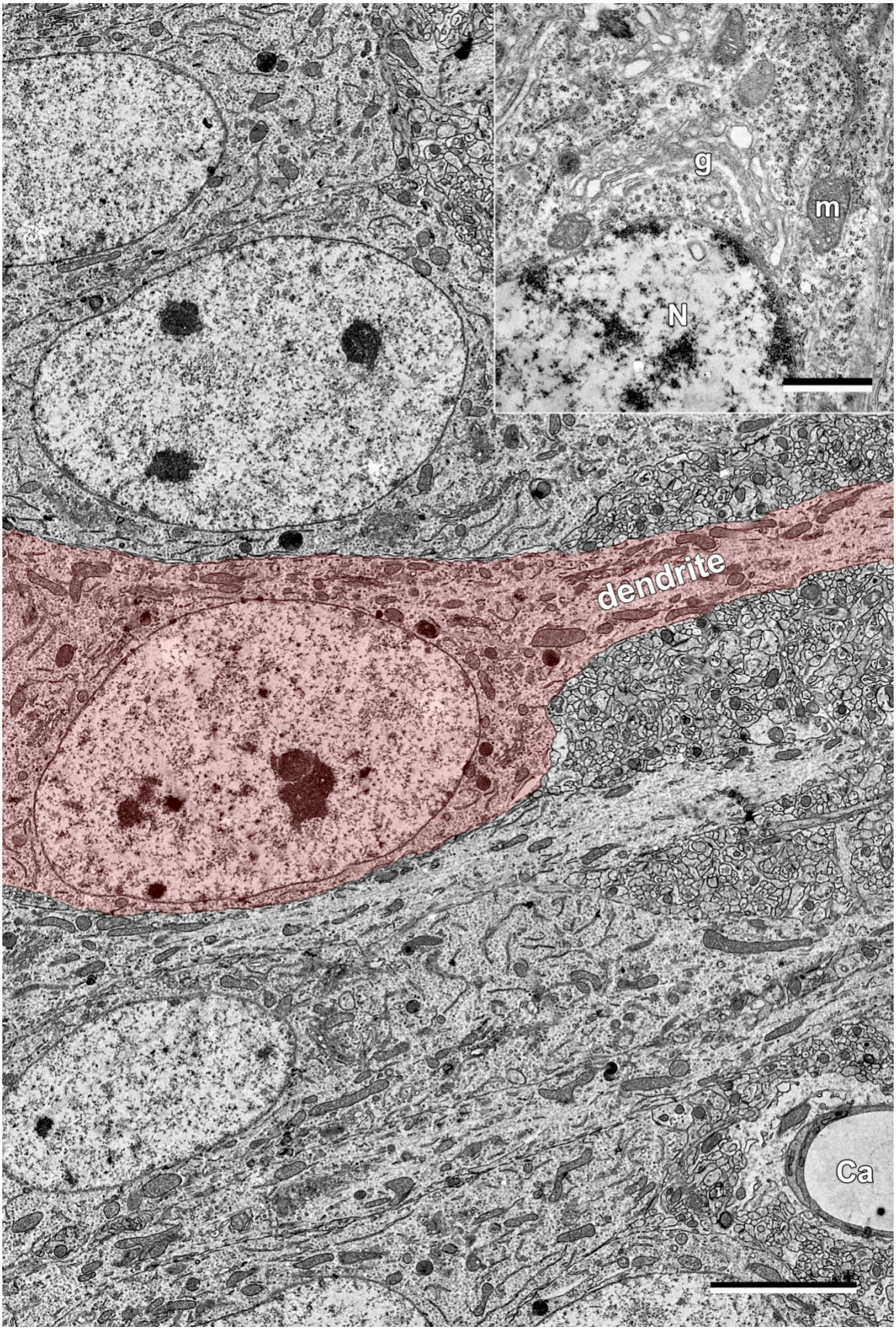
g
m
N
dendrite
Ca

Figure 9: Ultrastructure of CA1 pyramidal neurons. TEM of the PCL in the CA1 from a WT P21 mouse. Apical dendrites project from pyramidal cells into the SR. An example is shaded red. Scale bar = 5 μm. *Inset:* Higher magnification TEM of the perikaryon of a pyramidal neuron, indicating the nucleus (N), golgi apparatus (g), and mitochondria (m). Note the small capillary (Ca) with an intact and compact blood-brain barrier. Scale bar = 2 μm.

2.4.2 Synapse density and post-synaptic density lengths

Synapse densities were estimated from counting frames generated from ROIs. Panoramic images of ROIs were loaded into Photoshop (Adobe) and randomly sampled with a grid overlay. Square sample frames with side lengths of 10 μm plus 1 μm overhang were acquired and saved as separate files for analysis (5 per animal). Sample frames were bounded by Gundersen's unbiased counting frame with two inclusion boundaries and two exclusion boundaries (Gundersen, 1977). For estimates of synapse density, synapses with PSDs that intersected the left or bottom sides of the frame were not counted. Likewise, for estimates of PSD lengths, PSDs that intersected with the left or bottom sides of the frame were not counted (figure 11). Synapses were counted and PSD lengths were traced and measured in ImageJ using ROI manager (NIH). Counts and cumulative sums were then averaged, first by animal and then by group.

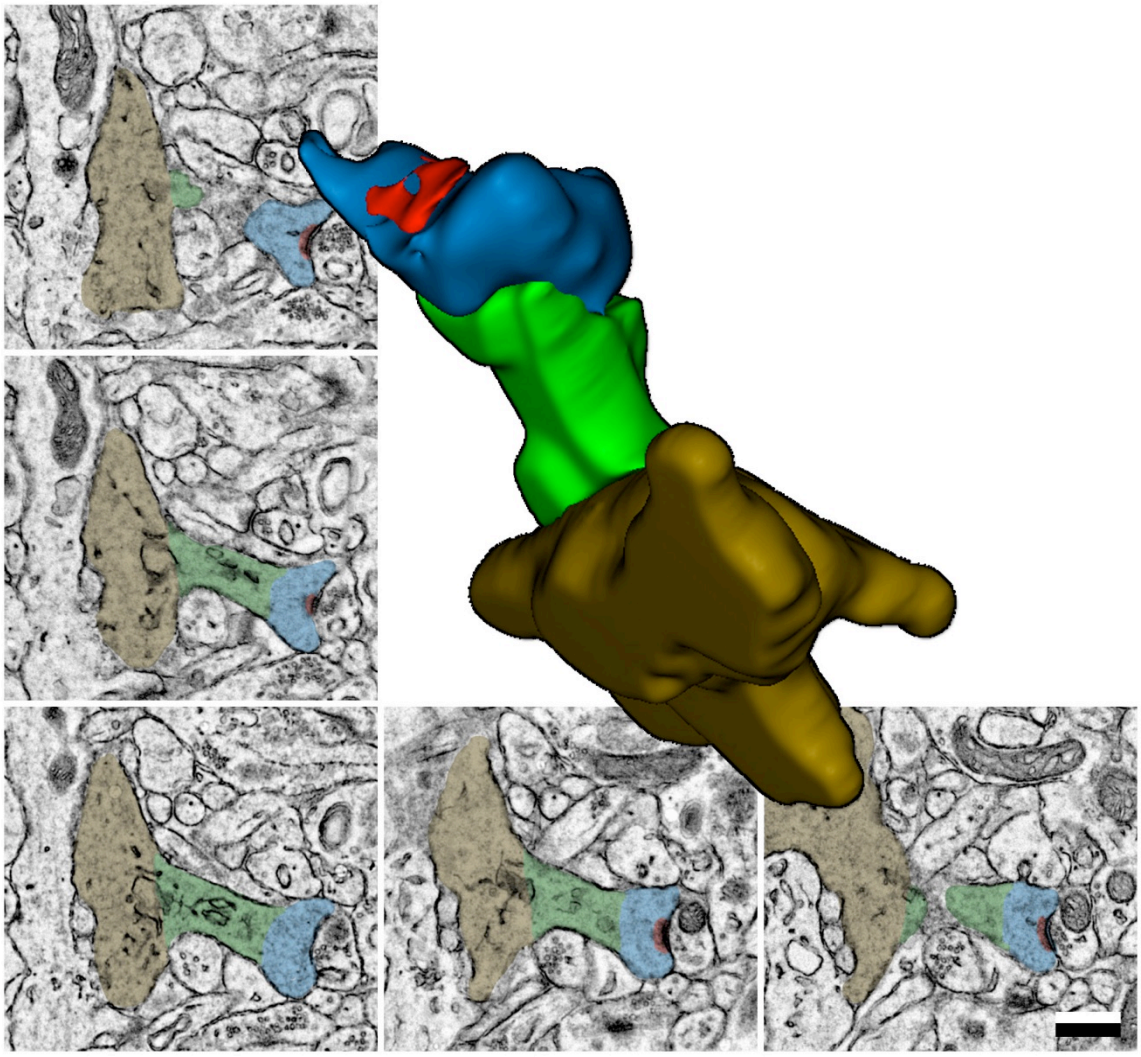

Figure 10: ssTEM of a dendritic spine from the DG MML of a WT P21 mouse. Five continuous serial sections (70 nm thick) of a spine have the PSD (red), spine head (blue), neck (green), and parent dendrite (brown) highlighted. In the center is a reconstruction of the spine generated in the TrakEM2 extension of ImageJ (NIH). Scale bar = 500 nm.

2.4.3 Dendritic spine morphometric analyses

Spines that met the selection criteria for morphometric analysis were identified in panoramic montages of the ROI. The morphological features measured were the spine neck width, spine neck length, and spine head width. The delineative criteria for these parameters may be well compared to those of a kitchen funnel. The spine neck width estimate was measured as the minimum diameter of the spine profile, or the narrowest aspect of the funnel. The spine neck length was determined using the polyline function in

ImageJ by measuring the distance from the base of the spine to the base of the head. This would be analogous to a measurement from the base of the funnel neck to the bottom of the funnel bowl. The spine head width was measured as the longest profile of the spine head, irrespective of its orientation to the neck. Similarly, one might measure the longest straight line possible within the opening of a funnel.

2.4.4 Estimating the resistance of the spine neck

The spine neck is thin and generally cylindrical and acts as the conduit for exchange between the spine head and the parent dendrite. Spine necks act as a bottleneck, providing resistance to the current passing from the spine head to the parent dendrite. The resistance of the spine neck (R_{neck}) may be estimated on the basis of neck morphometrics measured from electron micrographs (Alvarez and Sabatini, 2007):

$$R_{morph} = \rho L / A \qquad (1)$$

In this model, ρ is the resistivity of the cytoplasm, L the spine neck length, and A the cross-sectional area of the spine neck. Assuming that the neck is cylindrical, the cross-sectional area of the neck may be calculated from the minimum width of the spine neck. Reformulated with the measured morphometric values and resistivity as constant, the model for neck resistance may be calculated as:

$$R_{morph} = L / \pi (W_{min} / 2)^2 \qquad (2)$$

In this equation, W_{min} is the minimal width of the neck, so only the measured variables neck length and neck width are needed to estimate the resistance of the spine neck.

2.4.5 Statistical analyses

Differences in synapse density means and PSD length means were evaluated by Students t-test. Two-way ANOVA tests were also performed against subregion and genotype. Morphometric distributions were determined to be non-parametric using Lilliefors test for normality. Therefore, all morphometric distributions were compared using Mann-Whitney *U* test, which tests the null hypothesis that two populations are the same with no assumptions about the normality of distributions (Mann and Whitney, 1947). All analyses were performed using Python (numerical python, pandas). All plots were generated using Python extension matplotlib.

Results

3.1 Overview

Qualitative examination at the light microscopic level of toluidine blue-stained sections of the CA1 and DG from P21 male mice revealed no obvious differences in the overall cellular architecture and molecular layers between WT and *Fmr1*- animals. Similarly, at the electron microscopic level, no obvious qualitative differences were observed between WT and *Fmr1*- animals hippocampal subregions.

3.2 Synapse densities and PSD lengths are not different between WT and *Fmr1*- mice

Synapse densities and PSD lengths were measured from counting frames sampled from panoramic TEMs. It was found that synapse densities and the cumulative lengths of PSDs were not significantly different between WT and *Fmr1*- mice in both the DG and the SR regions of the hippocampus of P21 male mice (figure 11 and table 1). A two-way ANOVA determined that region was a significant source of variance for PSD length ($F = 13.87$; $p = 0.029$), with the SR having longer PSD lengths than the DG across genotype.

Table 1: Summary table of measured synapse densities and PSD lengths from the neuropil of DG and SR subfields in WT and *Fmr1*- P21 mice.

		WT	*Fmr1*-	p-value (t-test)
***N* (animals/frames)**	**DG**	5/10	4/10	--
	SR	4/10	3/10	--
Synapse density (synapses/100 μm^2)	**DG**	32.3 ± 4	30.3 ± 1	0.655
	SR	34.4 ± 2	30.7 ± 1	0.271
PSD length (μm/100 μm^2)	**DG**	5.7 ± 0.3	6.2 ± 0.9	0.628
	SR	7.6 ± 0.9	7.0 ± 0.3	0.621

3.3 Quantitative analysis of spine morphological parameters

The morphology of dendritic spines from the MML of DG granular cells and the SR of CA1 pyramidal cells were then carefully analyzed and compared in WT and *Fmr1*- animals. Prior to analyses, we measured the minimum spine neck diameters and maximum spine head diameters from a series of TEMs (figure 10) to determine if reliable estimates of spine neck widths and lengths and spine heads may be derived from

continuous two-dimensional profiles that met our criteria. Spine neck widths had an average deviation of 10 nm between sections; spine lengths had an average deviation of 8 nm; and spine heads had an average deviation of 31 nm (n = 10 spines).

The quantitative morphological analysis from two-dimensional sections revealed broad non-parametric distributions of the morphologies of spine necks and heads (see summary table below). Regression analyses comparing morphological parameters (neck length v. neck width; neck length v. head width; neck width v. head width) determined that there were no significant correlations between the parameters (see figures 21-23 in Appendix D). Slope coefficients were all between –1 and 1 (m = -0.03; 0.11; 0.3; r^2 = 0.621; 0.518; 0.695). In the absence of significant relationships between neck and head morphologies, it would be misleading to assign spines to categories like *mushroom, thin,* or *stubby*, in contrast to the groupings of spines previously used in the literature (Grossman et al, 2008; Harris et al., 1992). Therefore, our statistical analyses were performed on all of the spines collectively, as our results indicate that dendritic spines in the CA1 and DG exhibit a continuum of morphologies.

Table 2: Summary table of morphological data of dendritic spines collected from the neuropil of CA1 SR and DG subfields in WT and *Fmr1*- P21 mice. CI: confidence interval.

Morphological parameters	**WT**	***Fmr1-***
CA1 SR		
N (animals/spines)	4/176	3/200
Head width		
Range	201 – 1166 nm	163 – 1238 nm
Mean ± SE	524 ± 14 nm	515 ± 14 nm
95% CI on mean	497 – 552 nm	487 – 544 nm
Median ± SD	496 ± 187 nm	471 ± 202 nm
Neck length		
Range	95 – 1058 nm	103 – 1570 nm
Mean ± SE	421 ± 15 nm	425 ± 17 nm
95% CI on mean	392 – 451 nm	391 – 458 nm
Median ± SD	394 ± 200 nm	362 ± 239 nm
Neck width		
Range	41 – 434 nm	41 – 480 nm
Mean ± SE	162 ± 5 nm	161 ± 6 nm
95% CI on mean	152 – 172 nm	149 – 173 nm
Median ± SD	144 ± 65 nm	140 ± 86 nm
DG MML		
N (animals/spines)	5/240	4/200
Head width		
Range	80 – 1655 nm	181 – 1239 nm
Mean ± SE	525 ± 16 nm	529 ± 14 nm
95% CI on mean	193 – 556 nm	512 – 557 nm
Median ± SD	455 ± 249 nm	510 ± 198 nm
Neck length		
Range	85 – 1527 nm	62 – 1714 nm
Mean ± SE	457 ± 16 nm	485 ± 19 nm
95% CI on mean	426 – 488 nm	448 – 522 nm
Median ± SD	396 ± 244 nm	425 ± 265 nm
Neck width		
Range	52 – 574 nm	29 – 592 nm
Mean ± SE	193 ± 6 nm	167 ± 6 nm
95% CI on mean	181 – 206 nm	154 – 180 nm
Median ± SD	170 ± 96 nm	140 ± 91 nm

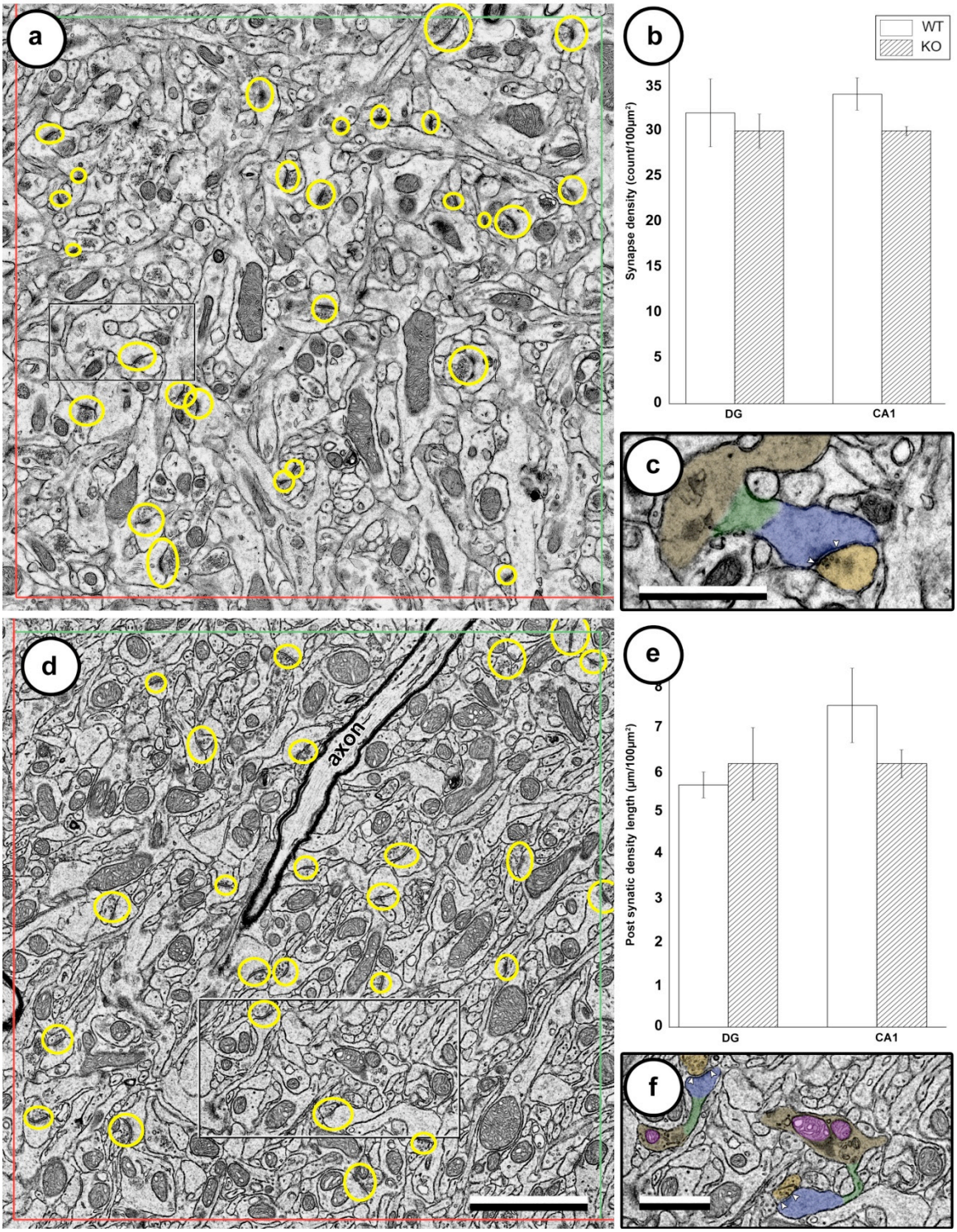
a
b
WT
KO
Synapse density (count/100μm²)
35
30
25
20
15
10
5
0
DG
CA1
c
d
axon
e
Post synatic density length (μm/100μm²)
7
6
5
4
3
2
1
0
DG
CA1
f

Figure 11: Quantification of synapse density and PSD lengths. Examples of WT (a) and *Fmr1-* (d) counting frames used for quantifying synapse densities (b) and post-synaptic density (PSD) lengths per area (e). The green and red borders indicate the counting frame, wherein synapses or PSDs intersecting with green borders are included while those intersecting red borders are excluded from the frame count. (c, f) Continuous dendritic spine profiles used in morphological analyses were pseudocoloured to highlight their ultrastructural features including mitochondria (pink), the parent dendrite (brown) with the protruding spine necks (green), spine heads (blue), receptor-anchoring PSDs (between arrowheads), and opposing pre-synaptic terminals (yellow). Scale bar = 2 μm. Inset scale bars = 1 μm.

3.4 WT DG MML spine necks are wider than CA1 SR spine necks

As the CA1 SR and DG MML have dendrites and synapses originating from different principal neurons with different morphologies and connectivities, it was hypothesized that regional differences exist in the ultrastructural characteristics of the dendritic spines. We found that spine necks were significantly wider in the DG, whereas no differences were detected between their neck lengths or head widths (figure 13).

3.5 Spine necks are narrower in the DG MML but not the CA1 SR of *Fmr1-* mice

It was then questioned whether the absence of FMRP affects spine morphologies in *Fmr1-* mice. In this study, it was observed that the distributions of spine neck widths are significantly narrower in the DG MML (figure 14) but not the CA1 SR (figure 15) of P21 *Fmr1-* mice when compared to WT controls. No significant difference between the neck lengths or head widths was observed between the groups.

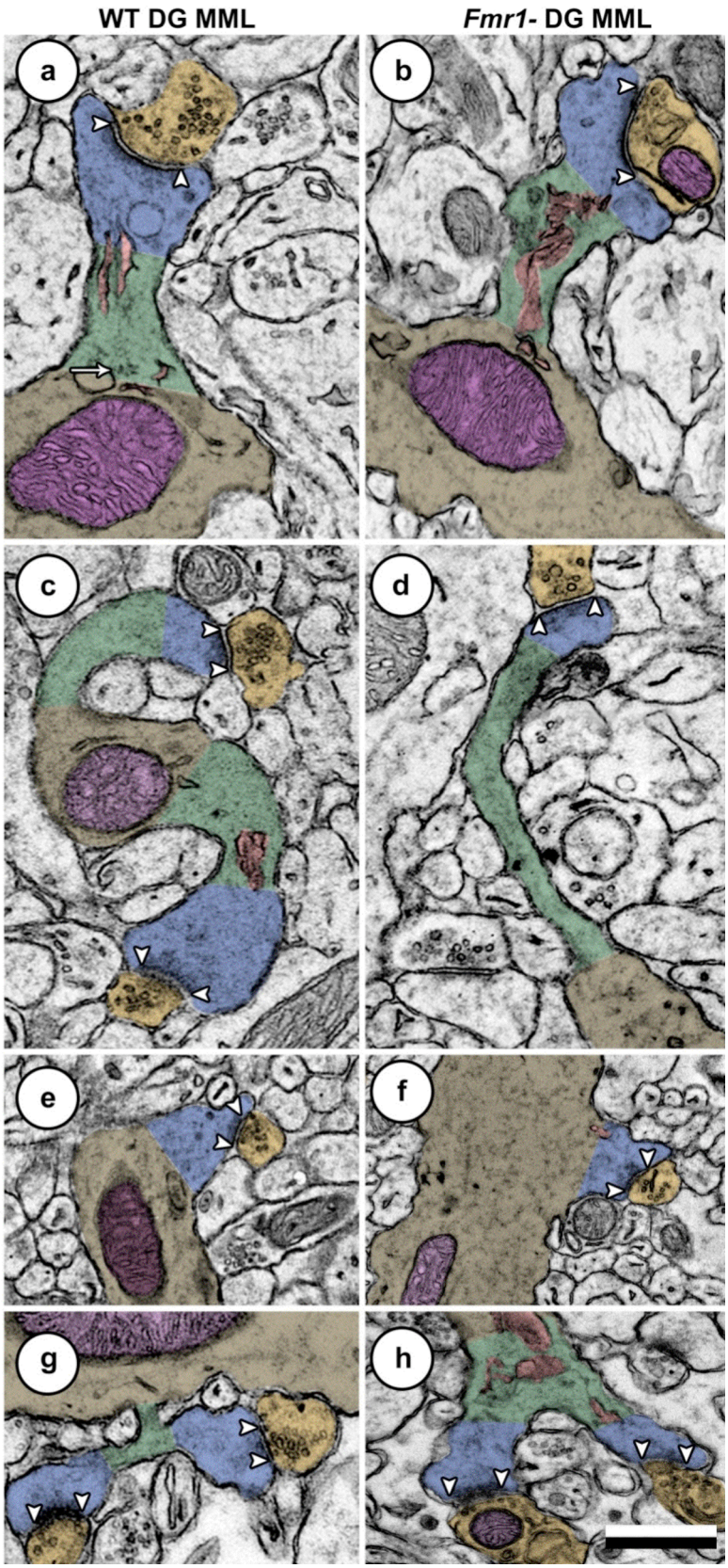
WT DG MML
Fmr1- DG MML
a
b
c
d
e
f
g
h

Figure 12: Spines present wide variation in their morphologies. Spines may have large heads (a, b); small heads (c); long necks (d); and other morphologies, including stubby spines (e, f) where necks would provide little resistance to the fluid or electrical flow from the spine head to the dendritic shaft. Continuous profiles of branched spines (g, h) were occasionally observed in all conditions. Spines were pseudocoloured to illustrate their ultrastructural features including mitochondria (pink), the parent dendrite (brown) with the protruding spine necks (green), spine heads (blue), and receptor-anchoring PSDs (between arrowheads), and opposing pre-synaptic terminals (yellow). Scale bar = 500 nm.

3.6 Spine neck resistance is greater in the DG MML of *Fmr1-* mice

Spine neck resistance is a combined test statistic, incorporating both the neck length and width. It is an important consideration because if narrow spines were also shorter, then their R_{neck} does not change significantly, suggesting no functional change. We found that spines of the *Fmr1-* DG MML had significantly higher R_{neck} values than WT (figure 16) and found no difference in the spines of the CA1 SR (figure 17).

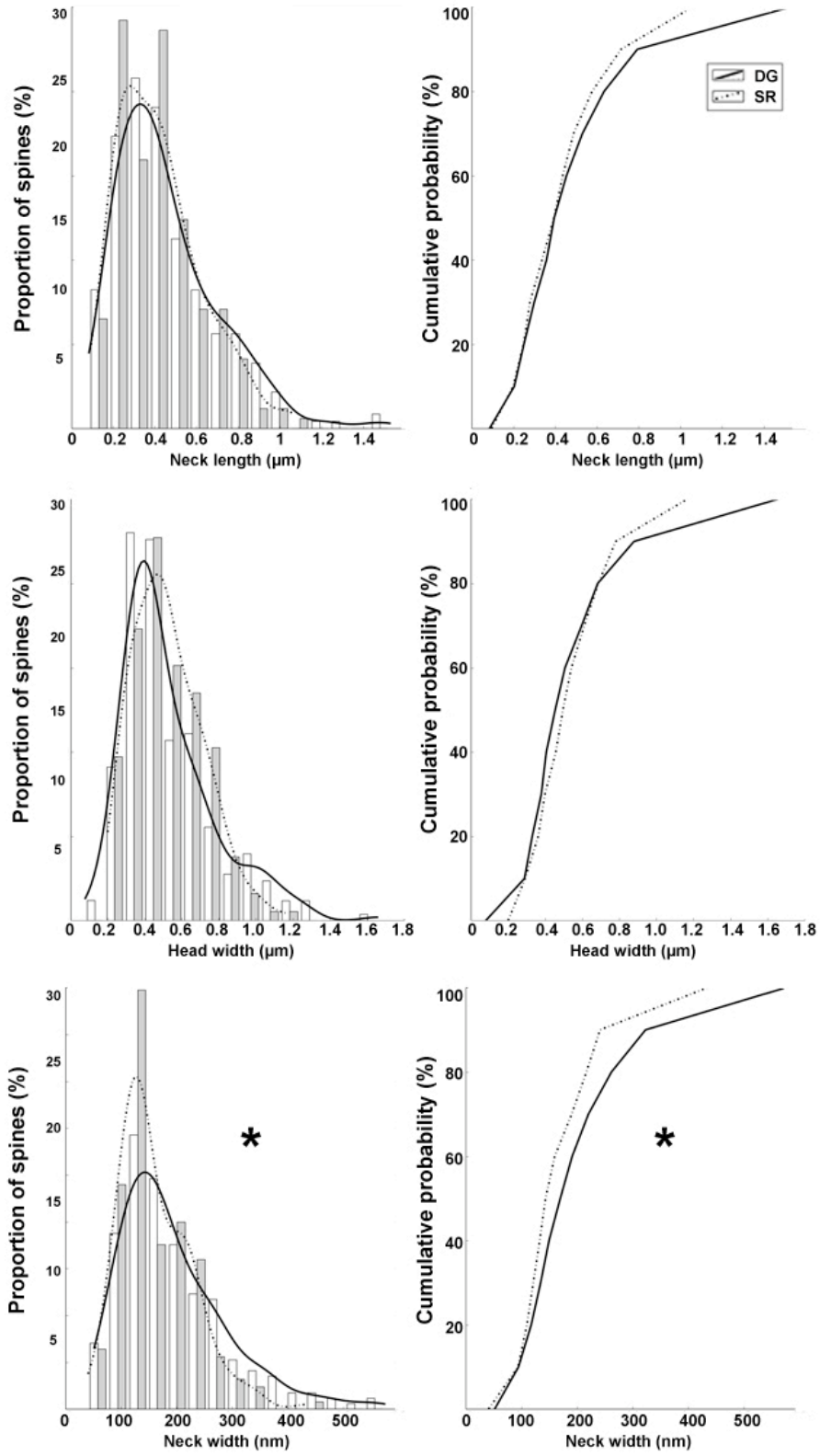
Proportion of spines (%)
Neck length (µm)
Cumulative probability (%)
DG
SR
Head width (µm)
Neck width (nm)
*
*

Figure 13: Comparison of DG MML and CA1 SR spine morphometrics. Distributions of neck lengths (top), head widths (middle) and neck widths (bottom) in the DG (unshaded bars) and CA1 (shaded bars) regions of WT mice. *Left:* Histograms of morphological data overlaid by a kernel-density estimate of the binned data. *Right:* Cumulative probability curves. Asterisk denotes statistically different distributions according to a Mann-Whitney *U* test with a significance level (α) less than 0.01.

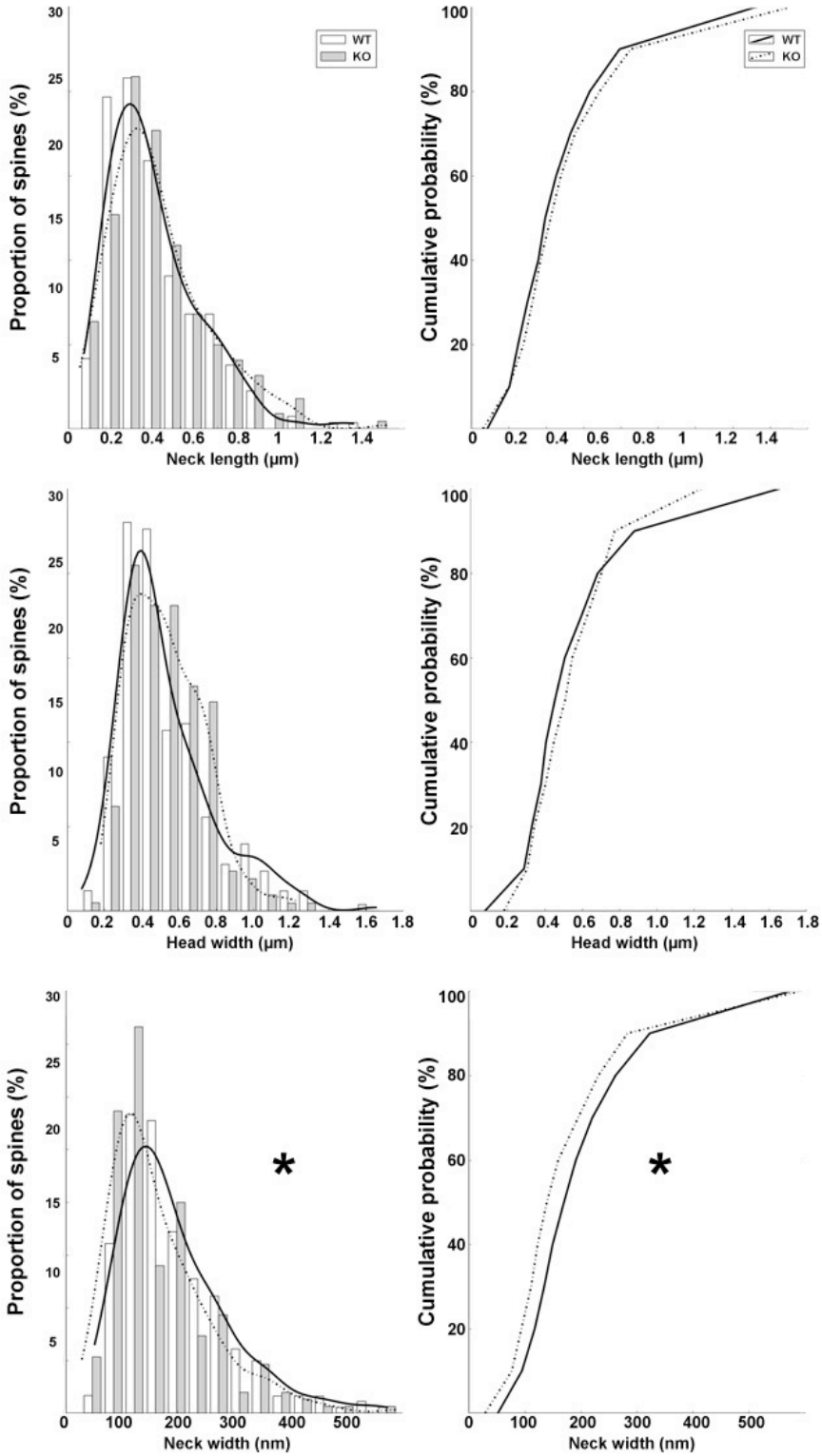

Figure 14: Morphometric analysis of dendritic spines from the DG MML. Distributions of neck lengths (top), head widths (middle) and neck widths in WT and *Fmr*- (KO) mice. *Left:*

Histograms of morphological data overlaid by a kernel-density estimate of the binned data. *Right:* Cumulative probability curves. Asterisk denotes statistically different distributions according to a Mann-Whitney *U* test with a significance level ($\propto$) less than 0.01.

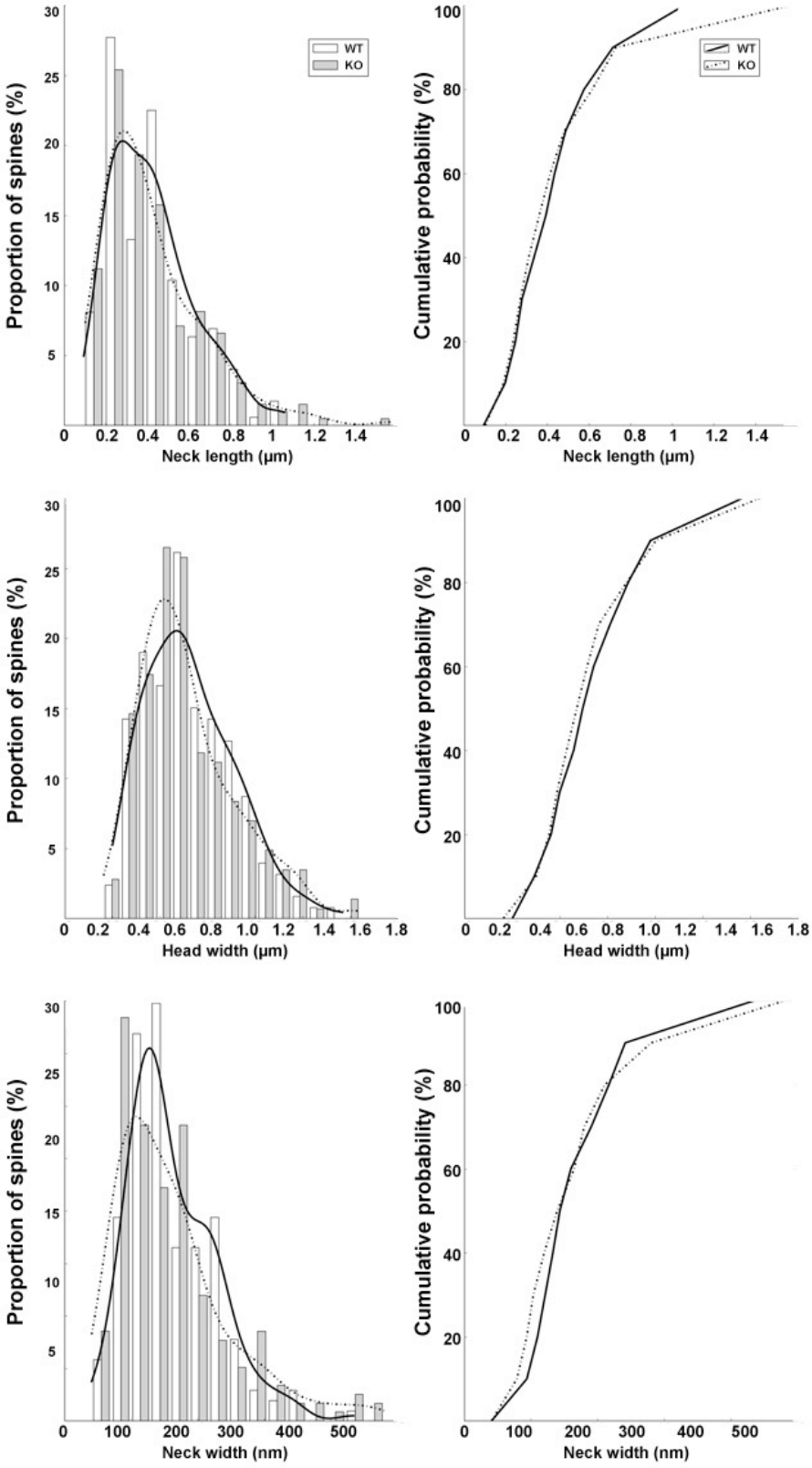
Proportion of spines (%)
WT
KO
Neck length (µm)
Cumulative probability (%)
WT
KO
Neck length (µm)
Proportion of spines (%)
Head width (µm)
Cumulative probability (%)
Head width (µm)
Proportion of spines (%)
Neck width (nm)
Cumulative probability (%)
Neck width (nm)

Figure 15: Morphological analysis of dendritic spines from the CA1 SR. Morphometric distributions of neck lengths (top), head widths (middle) and neck (bottom) widths. *Left:* Histograms of morphological data overlaid by a kernel-density estimate of the binned data. *Right:* Cumulative probability curves.

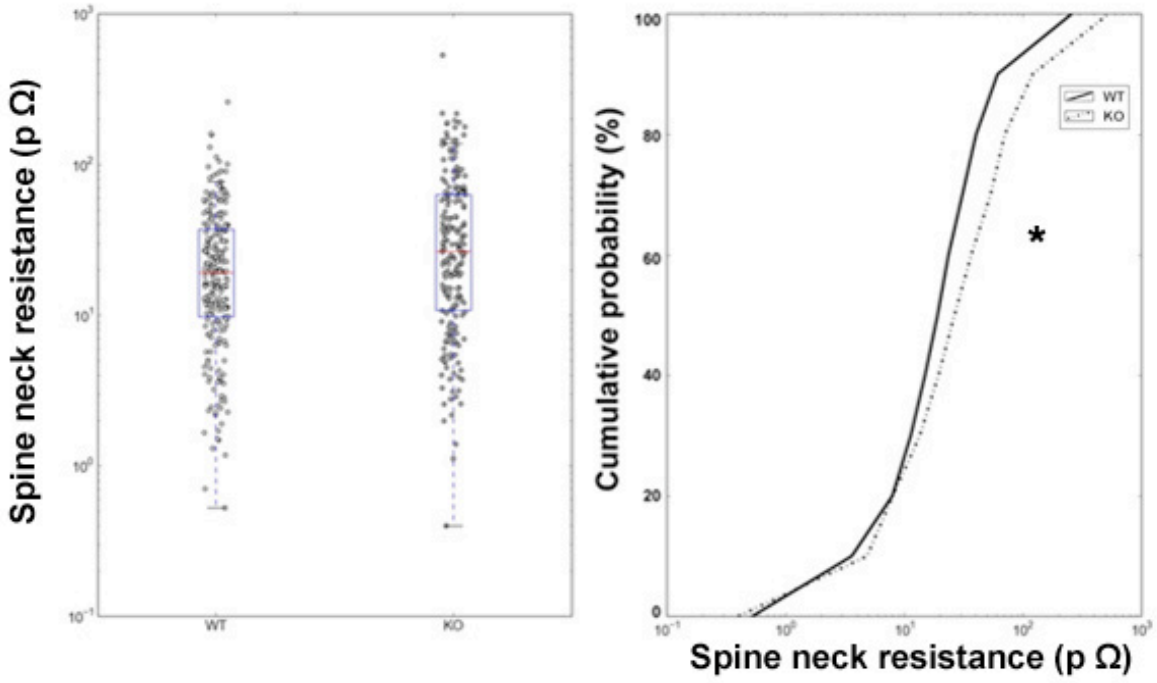

Figure 16: Estimated resistances of dendritic spine necks in the DG MML. *Left:* Scatter plot of estimated resistance overlaid by a box plot. *Right:* Semi-log cumulative probability curves. Asterisk denotes statistically different distributions according to a Mann-Whitney *U* test with a significance level ($\propto$) less than 0.01

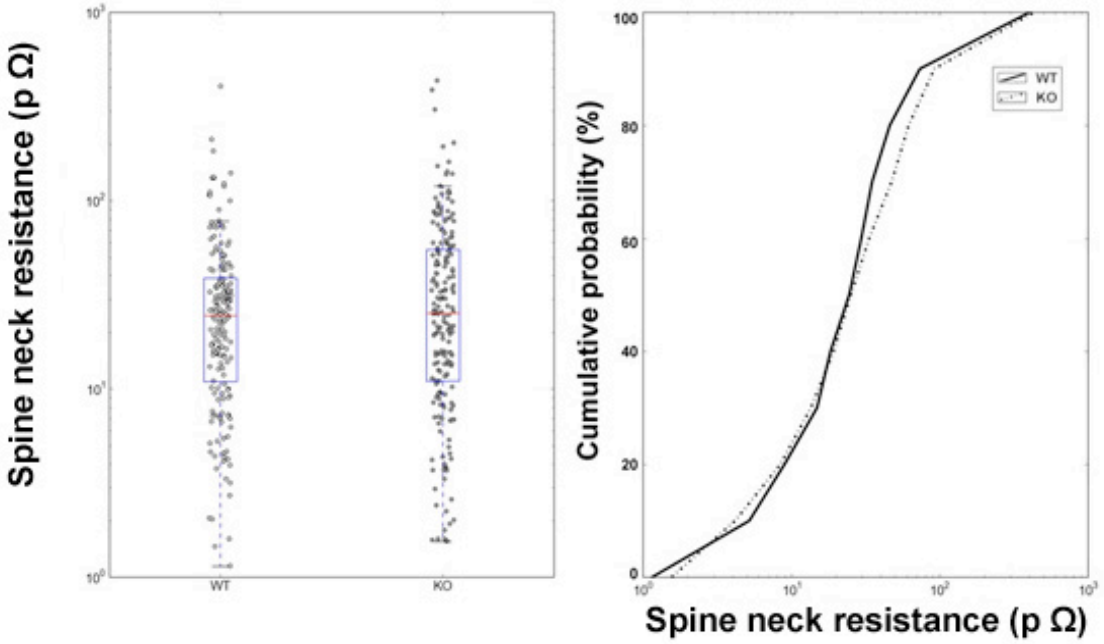

Figure 17: Estimated resistances of dendritic spine necks in the CA1 SR. *Left:* Scatter plot of estimated resistance overlaid by a box plot. *Right:* Semi-log cumulative probability curves. No significant differences were observed in spine necks of CA1 SR dendrites.

Discussion

Synapse densities, PSD lengths and area, and spine morphometrics from WT and *Fmr1*- male P21 mice were determined from wide-field TEM image montages of the DG MML and the CA1 SR. Of significance and importance, it was found that spine neck widths were significantly narrower in the *Fmr1*- DG compared to WT suggesting a regionally-specific role for FMRP in determining spine morphology and electrical resistance.

4.1 Reliable estimates of spine morphologies from two-dimensional profiles

In the morphometric component of this study we compared the distributions of the minimal neck widths, neck lengths and maximal head widths of dendritic spines. These parameters were measured from the two-dimensional profiles of three-dimensional spines. This approach provided more precise measurements when compared to confocal or stimulated-emission-depletion (STED) microscopy and is far less time consuming than serial section TEM (ssTEM) reconstructions.

Confocal and STED microscopy are both diffraction-limited techniques. Confocal microscopy is truly diffraction limited, wherein light passing through tissue is diffracted and produces a signal with a volume greater than its true magnitude. This limitation may be represented as a point spread function (PSF) and can be measured using fluorescent microspheres of a known size. The resolution limit of traditional confocal microscopy is 100-150 nm and is proportional to the emitted wavelengths of light. In confocal microscopy, the excitation of fluorophores surrounding the point of interest expands the PSF of the emitted signal. STED microscopy circumvents this effect by depleting the surrounding fluorophores using a toroid laser prior to imaging the point of interest, effectively increasing the resolution to 50-100 nm. A recent STED study of *Fmr1*- hippocampus found regionally- and age-dependent reduced neck widths in CA1 pyramidal neurons (Wijetunge et al., 2014). Two-photon and other multi-photon microscopic iterations have greater penetrative capacity than confocal or STED techniques but have similar resolution limits to confocal. However, spine morphometrics and other sub-cellular phenomena fall towards the lower bound of the resolution limits of these techniques, making robust analysis challenging.

Light microscopic techniques are most useful when imaging living tissue, as in longitudinal *in vivo* two-photon imaging through a cranial window, *in vitro* in acute slices or cultured cells, or in *ex vivo* explants (*e.g.*, whole-mount retina preparations). Studies using these techniques have elucidated many dynamic spine behaviours and have been used to describe spine phenotypes in FXS, including increased turnover of spines in cortical neurons (Cruz-Martín et al., 2010). However, these techniques ultimately lack the resolving capability required for precise measurements of spine necks and in determining the presence or absence of other subcellular organelles.

The most precise analyses of spine morphology and ultrastructure come from ssTEM reconstructions (Harris and Stevens, 1989). Traditionally, a ribbon of serial sections is collected on a slot grid and an ROI is captured from each section. Section thickness is calculated and reconstructions are rendered from manual tracings of features of interest (e.g., spines, endoplasmic reticulum). These reconstructions provide a lateral resolution of less a nanometer (dependent upon the quality of the microscope and the skills of the microscopist) and an axial resolution of the section thickness, typically 50-100 nm. In studies investigating spine morphometrics, resolution is not a limiting factor when employing ssTEM. However, the number of spines analyzed in these studies is usually in the tens, as the capture, alignment, tracing, reconstruction and analysis of dendritic segments is labour intensive and time consuming.

Our measurements were congruent with the measured values reported from serial section TEM (ssTEM) reconstructions of similar tissue (Harris and Stevens, 1989) and had comparable distributions to a STED study of spine morphologies of CA1 pyramidal neurons (Wijetunge et al., 2014), even though the P21 time point is different to both studies. However, the methods used in this study are far faster than traditional ssTEM experiments and more precise than light microscopic techniques. Thus, using two-dimensional profiles is a useful compromise of precision and throughput for the investigation of dendritic spine necks.

4.2 Reliable estimates of neck resistance from two-dimensional profiles

Previous ssTEM and diffusion studies of dendritic spines have reported a range of 1 to more than 500 MΩ for R_{neck} (Harris and Stevens, 1989; Svoboda et al., 1996; Harnett et al., 2012; Tonnesen et al., 2014). Data generated in this study from two-dimensional

TEM profiles of dendritic spines demonstrated a comparable distribution (0.4 – 530 MΩ with a resistivity (ρ) of 100Ω cm as used in Harris and Stevens, 1989 and Tonnesen et al., 2014).

4.3 Functional impact of reduced neck widths

Spine head and neck morphologies facilitate biochemical and electrical compartmentalization. The compartmentalization of molecular signals is positively correlated with head volume and negatively correlatied with R_{neck}. Electrical compartmentalization of current within the spine head is very sensitive to R_{neck}, where a 50% drop in R_{neck} would drop the spine EPSP by 20%-40% without significantly changing the dendritic EPSP, affecting the probabilities of activating voltage sensitive channels (Tonnesen et al., 2014).

The level of depolarization within the spine head is relatively independent of the diameter of its parent dendrite. However, the size of synaptic depolarization in the dendritic compartment will vary dramatically (increasing 30 fold from trunk to distal dendrites in CA1 pyramidal neurons) due to proportional changes in the impedance in dendrites of different diameters. This effect facilitates the relative location independence of dendritic EPSP and supports that R_{neck} does not vary according to dendritic compartment (Harnett et al., 2012).

Under normal conditions, LTP is associated with the enlargement of spine heads and correlative shortening and widening of spine necks. Thus, under normal LTP conditions biochemical compartmentalization would not change significantly (the changes in head and neck morphologies would equilibrate) but R_{neck} would drop significantly, thereby potentially reducing the probability of activating voltage-gated channels in the spine head (Tonnesen et al., 2014) and potentially limiting receptor trafficking between the dendrite and the spine head (Hugel et al., 2009). As NMDA receptors are a primary mediator of synaptic plasticity and only detect the coincident signals of membrane depolarization and extracellular ligand binding (Furukawa et al., 2005), changes in compartmentalization are likely to affect synaptic plasticity. NMDA-receptor hypofunction has been described in *Fm1-* mice (Eadie et al., 2012), which may be in part attributable to morphological changes to dendritic spines. A deficit in heterosynaptic plasticity in *Fmr1-* mice suggests a deficit in the communication between synapses (Connor et al., 2011), however, the

relationships between R_{neck}, spine compartmentalization, and heterosynaptic plasticity in *Fmr1-* mice have yet to be investigated.

4.4 Limitations

Synapse density measurements. Synapse density is a notoriously difficult problem to solve and requires the utmost in stereological rigour to predict accurately. There is tremendous intra-animal and intra-group variability that must be resolved before assessing inter-group variability. Gundersen recommends to "do more less well," (Gundersen and Østerby, 1981) however the economy of the stereological techniques required to achieve robust statistical power for estimating synapse density is extremely challenging in the context of a Master's project. We conducted robust pilot studies: if a dramatic difference in synapse density or PSD lengths existed between groups, it would have been detected in our analyses. However, detecting the subtle differences by sampling thousands of synapses from a pool of many millions is not practical.

Representation of long spines. Spines with longer necks have a lower probability of having a continuous profile within the two-dimensional section and may be under represented in the reported distributions. This is particularly problematic in assessing the FXS phenotype of long "immature" spines. Future investigations should consider supplementary techniques such as fluorescent cell labelling (Dumitriu et al., 2011), to determine the distributions of spine neck lengths and to estimate spine densities along dendrites.

Calculating tau: estimating spine head volumes. A comparison of R_{neck} and time constants (tau) would be possible if accurate head volumes could be estimated (Tonnesen et al., 2014). However, the assumption that spine heads are spherical is not accurate so a comparison was not possible. This is a limitation in STED studies (Harnett et al., 2012; Tonnesen et al., 2014; Wijetunge et al., 2014) as well. Reliable determination of spine head shapes require rigorous 3D reconstructions or serial block face scanning with a scanning electron microscope (Denk and Horstmann, 2004).

4.5 Future Directions

Future experiments using the TEM capture and analysis methods used above may constructively add to the reported data and protocol in a number of ways. Conducting

similar experiments with more time points, more regions, and more spines analyzed would undoubtedly provide a more complete description of the *Fmr1*- spine phenotype than any currently available.

Fluorescence recovery after photobleaching (FRAP) experiments may be useful in determining the efficacy of pharmacological intervention to ameliorate the spine phenotype of FXS and to recapitulate the results of this study (Grunditz et al., 2008). As spine necks are narrower in the DG, one would expect to see longer time constants for the recovery of fluorophores from the dendritic compartment back into the head compartment.

Applying appropriate stereological techniques for quantifying absolute synapse densities, cell densities, blood vessel densities and distributions of other organelles may provide unexpected insights into of the FXS pathology. Semi-automated scanning block face electron microscopy analysis would surely provide the highest throughput and most detailed means for ultrastructural analyses (Morales et al., 2011) and I expect to see similar studies using this technique within the next few years.

4.6 Conclusions

Taken together, these findings suggest that FMRP plays a role in granular cell neuron spine neck structure and may influence signal propagation in a regionally-specific manner in the hippocampus.

Bibliography

Abbeduto, L. and R. J. Hagerman (1997). "Language and communication in fragile X syndrome." Mental Retardation and Developmental Disabilities Research Reviews**3**(4): 313-322.

Allingham-Hawkins, D. J., R. Babul-Hirji, D. Chitayat, J. J. Holden, K. T. Yang, C. Lee, R. Hudson, H. Gorwill, S. L. Nolin and A. Glicksman (1999). "Fragile X premutation is a significant risk factor for premature ovarian failure: the International Collaborative POF in Fragile X study—preliminary data." American journal of medical genetics**83**(4): 322.

Ashley, C. T., K. D. Wilkinson, D. Reines and S. T. Warren (1993). "FMR1 protein: conserved RNP family domains and selective RNA binding." Science**262**(5133): 563-566.

Bagni, C. and W. T. Greenough (2005). "From mRNP trafficking to spine dysmorphogenesis: the roots of fragile X syndrome." Nature Reviews Neuroscience**6**(5): 376-387.

Bassell, G. J. and S. T. Warren (2008). "Fragile X syndrome: loss of local mRNA regulation alters synaptic development and function." Neuron**60**(2): 201-214.

Bastrikova, N., G. A. Gardner, J. M. Reece, A. Jeromin and S. M. Dudek (2008). "Synapse elimination accompanies functional plasticity in hippocampal neurons." Proceedings of the National Academy of Sciences**105**(8): 3123-3127.

Bear, M. F., K. M. Huber and S. T. Warren (2004). "The mGluR theory of fragile X mental retardation." Trends in neurosciences**27**(7): 370-377.

Berkley, J. (1895). "Studies on the lesions produced by the action of certain poisons on the nerve-cell." Med News**67**: 225-231.

Bilousova, T., L. Dansie, M. Ngo, J. Aye, J. R. Charles, D. W. Ethell and I. M. Ethell (2009). "Minocycline promotes dendritic spine maturation and improves behavioural performance in the fragile X mouse model." Journal of Medical Genetics**46**(2): 94-102.

Bourne, J. N. and K. M. Harris (2008). "Balancing structure and function at hippocampal dendritic spines." Annual review of neuroscience**31**: 47.

Castets, M., C. Schaeffer, E. Bechara, A. Schenck, E. W. Khandjian, S. Luche, H. Moine, T. Rabilloud, J.-L. Mandel and B. Bardoni (2005). "FMRP interferes with the Rac1 pathway and controls actin cytoskeleton dynamics in murine fibroblasts." Human molecular genetics**14**(6): 835-844.

Chen, E., M. R. Sharma, X. Shi, R. K. Agrawal and S. Joseph (2014). "Fragile X mental retardation protein regulates translation by binding directly to the ribosome." Molecular cell**54**(3): 407-417.

Cingolani, L. A. and Y. Goda (2008). "Actin in action: the interplay between the actin cytoskeleton and synaptic efficacy." Nature Reviews Neuroscience**9**(5): 344-356.

Cohen, R. S., F. Blomberg, K. Berzins and P. Siekevitz (1977). "The structure of postsynaptic densities isolated from dog cerebral cortex: I. overall morphology and protein composition." The Journal of cell biology**74**(1): 181-203.

Colak, D., N. Zaninovic, M. S. Cohen, Z. Rosenwaks, W.-Y. Yang, J. Gerhardt, M. D. Disney and S. R. Jaffrey (2014). "Promoter-bound trinucleotide repeat mRNA drives epigenetic silencing in fragile X syndrome." Science**343**(6174): 1002-1005.

Colledge, M., E. M. Snyder, R. A. Crozier, J. A. Soderling, Y. Jin, L. K. Langeberg, H. Lu, M. F. Bear and J. D. Scott (2003). "Ubiquitination regulates PSD-95 degradation and AMPA receptor surface expression." Neuron**40**(3): 595-607.

Comery, T. A., J. B. Harris, P. J. Willems, B. A. Oostra, S. A. Irwin, I. J. Weiler and W. T. Greenough (1997). "Abnormal dendritic spines in fragile X knockout mice: maturation and pruning deficits." Proceedings of the National Academy of Sciences**94**(10): 5401-5404.

Connor, S. A., C. A. Hoeffer, E. Klann and P. V. Nguyen (2011). "Fragile X mental retardation protein regulates heterosynaptic plasticity in the hippocampus." Learning & Memory**18**(4): 207-220.

Consortium, D.-B. F. X. (1994). "Fmr1 knockout mice: a model to study fragile X mental retardation. The Dutch-Belgian Fragile X Consortium." Cell**78**(1): 23-33.

Cruz-Martín, A., M. Crespo and C. Portera-Cailliau (2010). "Delayed stabilization of dendritic spines in fragile X mice." The Journal of Neuroscience**30**(23): 7793-7803.

Dailey, M. E. and S. J. Smith (1996). "The dynamics of dendritic structure in developing hippocampal slices." The Journal of neuroscience**16**(9): 2983-2994.

De Roo, M., P. Klauser, P. M. Garcia, L. Poglia and D. Muller (2008). "Spine dynamics and synapse remodeling during LTP and memory processes." Progress in brain research**169**: 199-207.

De Rubeis, S. and C. Bagni (2010). "Fragile X mental retardation protein control of neuronal mRNA metabolism: Insights into mRNA stability." Molecular and Cellular Neuroscience**43**(1): 43-50.

De Vries, B., C. Jansen, A. A. Duits, C. Verheij, R. Willemsen, J. Van Hemel, A. Van den Ouweland, M. Niermeijer, B. Oostra and D. Halley (1996). "Variable FMR1 gene methylation of large expansions leads to variable phenotype in three males from one fragile X family." Journal of medical genetics**33**(12): 1007-1010.

Deller, T., C. B. Orth, D. Del Turco, A. Vlachos, G. J. Burbach, A. Drakew, S. Chabanis, M. Korte, H. Schwegler and C. A. Haas (2007). "A role for synaptopodin and the spine apparatus in hippocampal synaptic plasticity." Annals of Anatomy-Anatomischer Anzeiger**189**(1): 5-16.

Denk, W. and H. Horstmann (2004). "Serial block-face scanning electron microscopy to reconstruct three-dimensional tissue nanostructure." PLoS biology**2**(11): e329.

Dictenberg, J. B., S. A. Swanger, L. N. Antar, R. H. Singer and G. J. Bassell (2008). "A direct role for FMRP in activity-dependent dendritic mRNA transport links filopodial-spine morphogenesis to fragile X syndrome." Developmental cell**14**(6): 926-939.

Dogiel, A. (1896). "Die Nervenelemente im Kleinhirne der Vögel und Säugethiere." Archiv für mikroskopische Anatomie**47**(4): 707-719.

Dölen, G. and M. F. Bear (2008). "Role for metabotropic glutamate receptor 5 (mGluR5) in the pathogenesis of fragile X syndrome." The Journal of physiology**586**(6): 1503-1508.

Dumitriu, D., A. Rodriguez and J. H. Morrison (2011). "High-throughput, detailed, cell-specific neuroanatomy of dendritic spines using microinjection and confocal microscopy." Nature protocols**6**(9): 1391-1411.

Eadie, B. D., J. Cushman, T. S. Kannangara, M. S. Fanselow and B. R. Christie (2012). "NMDA receptor hypofunction in the dentate gyrus and impaired context discrimination in adult Fmr1 knockout mice." Hippocampus**22**(2): 241-254.

Ethell, I. M. and E. B. Pasquale (2005). "Molecular mechanisms of dendritic spine development and remodeling." Progress in neurobiology**75**(3): 161-205.

Feng, Y., D. Absher, D. E. Eberhart, V. Brown, H. E. Malter and S. T. Warren (1997a). "FMRP associates with polyribosomes as an mRNP, and the I304N mutation of severe fragile X syndrome abolishes this association." Molecular cell**1**(1): 109-118.

Feng, Y., C.-A. Gutekunst, D. E. Eberhart, H. Yi, S. T. Warren and S. M. Hersch (1997b). "Fragile X mental retardation protein: nucleocytoplasmic shuttling and association with somatodendritic ribosomes." The Journal of neuroscience**17**(5): 1539-1547.

Ferri, R., S. Musumeci, M. Elia, S. Del Gracco, C. Scuderi and P. Bergonzi (1994). "BIT-mapped somatosensory evoked potentials in the fragile X syndrome." Neurophysiologie Clinique/Clinical Neurophysiology**24**(6): 413-426.

Fifkova, E. and M. Morales (1989). "Calcium_Regulated Contractile and Cytoskeletal Proteins in Dendritic Spines May Control Synaptic Plasticitya." Annals of the New York Academy of Sciences**568**(1): 131-137.

Fischer, M., S. Kaech, D. Knutti and A. Matus (1998). "Rapid actin-based plasticity in dendritic spines." Neuron**20**(5): 847-854.

Fu, M. and Y. Zuo (2011). "Experience-dependent structural plasticity in the cortex." Trends in neurosciences**34**(4): 177-187.

Fu, Y.-H., D. P. Kuhl, A. Pizzuti, M. Pieretti, J. S. Sutcliffe, S. Richards, A. J. Verkert, J. J. Holden, R. G. Fenwick and S. T. Warren (1991). "Variation of the CGG repeat at the fragile X site results in genetic instability: resolution of the Sherman paradox." Cell**67**(6): 1047-1058.

Fu, Y. H., D. P. Kuhl, A. Pizzuti, M. Pieretti, J. S. Sutcliffe, S. Richards, A. J. Verkerk, J. J. Holden, R. G. Fenwick, Jr., S. T. Warren and et al. (1991). "Variation of the CGG repeat at the fragile X site results in genetic instability: resolution of the Sherman paradox." Cell**67**(6): 1047-1058.

Galvez, R. and W. T. Greenough (2005). "Sequence of abnormal dendritic spine development in primary somatosensory cortex of a mouse model of the fragile X mental retardation syndrome." American journal of medical genetics Part A**135**(2): 155-160.

Gerlach, J. v. (1872). "The spinal cord." Manual of histology (ed. S. Stricker): 327-366.

Gray, E. (1959). "Electron microscopy of synaptic contacts on dendrite spines of the cerebral cortex."

Gray, E. G. (1959). "Axo-somatic and axo-dendritic synapses of the cerebral cortex: an electron microscope study." Journal of anatomy**93**(Pt 4): 420.

Greco, C., R. Berman, R. Martin, F. Tassone, P. Schwartz, A. Chang, B. Trapp, C. Iwahashi, J. Brunberg and J. Grigsby (2006). "Neuropathology of fragile X-associated tremor/ataxia syndrome (FXTAS)." Brain**129**(1): 243-255.

Grossman, A. W., G. M. Aldridge, K. J. Lee, M. K. Zeman, C. S. Jun, H. S. Azam, T. Arii, K. Imoto and W. T. Greenough (2010). "Developmental characteristics of dendritic spines in the dentate gyrus of Fmr1 knockout mice." Brain research**1355**: 221-227.

Grossman, A. W., N. M. Elisseou, B. C. McKinney and W. T. Greenough (2006). "Hippocampal pyramidal cells in adult Fmr1 knockout mice exhibit an immature-appearing profile of dendritic spines." Brain research**1084**(1): 158-164.

Grunditz, Å., N. Holbro, L. Tian, Y. Zuo and T. G. Oertner (2008). "Spine neck plasticity controls postsynaptic calcium signals through electrical compartmentalization." The Journal of neuroscience**28**(50): 13457-13466.

Grutzendler, J., N. Kasthuri and W.-B. Gan (2002). "Long-term dendritic spine stability in the adult cortex." Nature**420**(6917): 812-816.

Gundersen, H. and R. Østerby (1981). "Optimizing sampling efficiency of stereological studies in biology: or 'Do more less well!'." Journal of Microscopy**121**(1): 65-73.

Gundersen, H. J. G. (1977). "Notes on the estimation of the numerical density of arbitrary profiles: the edge effect." Journal of microscopy**111**(2): 219-223.

Hagerman, R., G. Hoem and P. Hagerman (2010). "Fragile X and autism: intertwined at the molecular level leading to targeted treatments." Mol Autism**1**(1): 12.

Hagerman, R. J. (2002). "The physical and behavioral phenotype." Fragile X syndrome: Diagnosis, treatment, and research**3**: 206-248.

Hagerman, R. J., R. A. Schreiner, M. B. Kemper, M. D. Wittenberger, B. Zahn and K. Habicht (1989). "Longitudinal IQ changes in fragile X males." American Journal of Medical Genetics**33**(4): 513-518.

Halpain, S. (2000). "Actin and the agile spine: how and why do dendritic spines dance?" Trends in neurosciences**23**(4): 141-146.

Harlow, E. G., S. M. Till, T. A. Russell, L. S. Wijetunge, P. Kind and A. Contractor (2010). "Critical period plasticity is disrupted in the barrel cortex of FMR1 knockout mice." Neuron**65**(3): 385-398.

Harnett, M. T., J. K. Makara, N. Spruston, W. L. Kath and J. C. Magee (2012). "Synaptic amplification by dendritic spines enhances input cooperativity." Nature**491**(7425): 599-602.

Harris, K. M., F. E. Jensen and B. Tsao (1992). "Three-dimensional structure of dendritic spines and synapses in rat hippocampus (CA1) at postnatal day 15 and adult ages: implications for the maturation of synaptic physiology and long-term potentiation." J Neurosci**12**(7): 2685-2705.

Harris, K. M. and J. Stevens (1988). "Dendritic spines of rat cerebellar Purkinje cells: serial electron microscopy with reference to their biophysical characteristics." The Journal of neuroscience**8**(12): 4455-4469.

Harris, K. M. and J. K. Stevens (1989). "Dendritic spines of CA 1 pyramidal cells in the rat hippocampus: serial electron microscopy with reference to their biophysical characteristics." The Journal of neuroscience**9**(8): 2982-2997.

Harrison, C. J., E. M. Jack, T. D. Allen and R. Harris (1983). "The fragile X: a scanning electron microscope study." Journal of medical genetics**20**(4): 280-285.

Hessl, D., S. M. Rivera and A. L. Reiss (2004). "The neuroanatomy and neuroendocrinology of fragile X syndrome." Mental retardation and developmental disabilities research reviews**10**(1): 17-24.

Hinton, V., W. Brown, K. Wisniewski and R. Rudelli (1991). "Analysis of neocortex in three males with the fragile X syndrome." American journal of medical genetics**41**(3): 289-294.

Hodapp, R. M., E. M. Dykens, R. J. Hagerman, R. Schreiner, A. M. Lachiewicz and J. F. Leckman (1990). "Developmental implications of changing trajectories of IQ in males with fragile X syndrome." Journal of the American Academy of Child & Adolescent Psychiatry**29**(2): 214-219.

Holtmaat, A. and K. Svoboda (2009). "Experience-dependent structural synaptic plasticity in the mammalian brain." Nature Reviews Neuroscience**10**(9): 647-658.

Huber, K. M., S. M. Gallagher, S. T. Warren and M. F. Bear (2002). "Altered synaptic plasticity in a mouse model of fragile X mental retardation." Proceedings of the National Academy of Sciences**99**(11): 7746-7750.

Hugel, S., M. Abegg, V. De Paola, P. Caroni, B. H. Gähwiler and R. A. McKinney (2009). "Dendritic spine morphology determines membrane-associated protein exchange between dendritic shafts and spine heads." Cerebral Cortex**19**(3): 697-702.

Hunter, J., O. Rivero_Arias, A. Angelov, E. Kim, I. Fotheringham and J. Leal (2014). "Epidemiology of fragile X syndrome: A systematic review and meta_analysis." American Journal of Medical Genetics Part A**164**(7): 1648-1658.

Irwin, S. A., M. Idupulapati, M. E. Gilbert, J. B. Harris, A. B. Chakravarti, E. J. Rogers, R. A. Crisostomo, B. P. Larsen, A. Mehta and C. Alcantara (2002). "Dendritic spine and dendritic field characteristics of layer V pyramidal neurons in the visual cortex of fragile_X knockout mice." American journal of medical genetics**111**(2): 140-146.

Irwin, S. A., B. Patel, M. Idupulapati, J. B. Harris, R. A. Crisostomo, B. P. Larsen, F. Kooy, P. J. Willems, P. Cras and P. B. Kozlowski (2001). "Abnormal dendritic spine characteristics in the temporal and visual cortices of patients with fragile_X syndrome: a quantitative examination." American journal of medical genetics**98**(2): 161-167.

Jones, E. and T. Powell (1969). "Morphological variations in the dendritic spines of the neocortex." Journal of cell science**5**(2): 509-529.

Jung, K.-M., M. Sepers, C. M. Henstridge, O. Lassalle, D. Neuhofer, H. Martin, M. Ginger, A. Frick, N. V. DiPatrizio and K. Mackie (2012). "Uncoupling of the endocannabinoid signalling complex in a mouse model of fragile X syndrome." Nature communications**3**: 1080.

Kasai, H., M. Fukuda, S. Watanabe, A. Hayashi-Takagi and J. Noguchi (2010). "Structural dynamics of dendritic spines in memory and cognition." Trends in neurosciences**33**(3): 121-129.

Kasai, H., M. Matsuzaki, J. Noguchi, N. Yasumatsu and H. Nakahara (2003). "Structure–stability–function relationships of dendritic spines." Trends in neurosciences**26**(7): 360-368.

Khandjian, E. W., F. Corbin, S. Woerly and F. Rousseau (1996). "The fragile X mental retardation protein is associated with ribosomes." Nature genetics**12**(1): 91-93.

Kirov, S., L. Petrak, J. Fiala and K. Harris (2004). "Dendritic spines disappear with chilling but proliferate excessively upon rewarming of mature hippocampus." Neuroscience**127**(1): 69-80.

Koekkoek, S., K. Yamaguchi, B. Milojkovic, B. Dortland, T. Ruigrok, R. Maex, W. De Graaf, A. E. Smit, F. VanderWerf and C. Bakker (2005). "Deletion of FMR1 in Purkinje cells enhances parallel fiber LTD, enlarges spines, and attenuates cerebellar eyelid conditioning in Fragile X syndrome." Neuron**47**(3): 339-352.

Kolliker, A. v. (1896). "Handbuch der Gewebelehre des Menschen." Bd**2**: 835.

Kondo, S., S. Kohsaka and S. Okabe (2011). "Long-term changes of spine dynamics and microglia after transient peripheral immune response triggered by LPS in vivo." Mol Brain**4**: 27.

Krucker, T., G. R. Siggins and S. Halpain (2000). "Dynamic actin filaments are required for stable long-term potentiation (LTP) in area CA1 of the hippocampus." Proceedings of the National Academy of Sciences**97**(12): 6856-6861.

Lachiewicz, A. M., C. M. Gullion, G. A. Spiridigliozzi and A. S. Aylsworth (1987). "Declining IQs of young males with the fragile X syndrome." American Journal on Mental Retardation.

Laing, S., M. Partington, H. Robinson and G. Turner (1991). "Clinical screening score for the fragile X (Martin_Bell) syndrome." American journal of medical genetics**38**(2_3): 256-259.

Lavenex, P. and P. B. Lavenex (2013). "Building hippocampal circuits to learn and remember: insights into the development of human memory." Behavioural brain research**254**: 8-21.

Lendvai, B., E. A. Stern, B. Chen and K. Svoboda (2000). "Experience-dependent plasticity of dendritic spines in the developing rat barrel cortex in vivo." Nature**404**(6780): 876-881.

Levenga, J., F. M. de Vrij, R. A. Buijsen, T. Li, I. M. Nieuwenhuizen, A. Pop, B. A. Oostra and R. Willemsen (2011). "Subregion-specific dendritic spine abnormalities in the hippocampus of Fmr1 KO mice." Neurobiology of learning and memory**95**(4): 467-472.

Lubs, H. A. (1969). "A marker X chromosome." Am J Hum Genet**21**(3): 231-244.

Luo, L. (2002). "Actin cytoskeleton regulation in neuronal morphogenesis and structural plasticity." Annual review of cell and developmental biology**18**(1): 601-635.

Majewska, A., A. Tashiro and R. Yuste (2000). "Regulation of spine calcium dynamics by rapid spine motility." The Journal of Neuroscience**20**(22): 8262-8268.

Mann, H. B. and D. R. Whitney (1947). "On a test of whether one of two random variables is stochastically larger than the other." The annals of mathematical statistics: 50-60.

Marin-Padilla, M. (1972). "Structural abnormalities of the cerebral cortex in human chromosomal aberrations: a Golgi study." Brain research**44**(2): 625-629.

Martin, J. P. and J. Bell (1943). "A pedigree of mental defect showing sex-linkage." Journal of neurology and psychiatry**6**(3-4): 154.

Matsuzaki, M., G. C. Ellis-Davies, T. Nemoto, Y. Miyashita, M. Iino and H. Kasai (2001). "Dendritic spine geometry is critical for AMPA receptor expression in hippocampal CA1 pyramidal neurons." Nature neuroscience**4**(11): 1086-1092.

Matsuzaki, M., N. Honkura, G. C. Ellis-Davies and H. Kasai (2004). "Structural basis of long-term potentiation in single dendritic spines." Nature**429**(6993): 761-766.

Matus, A. (2000). "Actin-based plasticity in dendritic spines." Science**290**(5492): 754-758.

Matus, A. and D. Taff-Jones (1978). "Morphology and molecular composition of isolated postsynaptic junctional structures." Proceedings of the Royal Society of London. Series B. Biological Sciences**203**(1151): 135-151.

McKinney, B. C., A. W. Grossman, N. M. Elisseou and W. T. Greenough (2005). "Dendritic spine abnormalities in the occipital cortex of C57BL/6 Fmr1 knockout mice." American Journal of Medical Genetics Part B: Neuropsychiatric Genetics**136**(1): 98-102.

Meredith, R. M., C. D. Holmgren, M. Weidum, N. Burnashev and H. D. Mansvelder (2007). "Increased threshold for spike-timing-dependent plasticity is caused by unreliable calcium signaling in mice lacking fragile X gene FMR1." Neuron**54**(4): 627-638.

Miller, L., D. McIntosh, J. McGrath, V. Shyu, M. Lampe, A. Taylor, F. Tassone, K. Neitzel, T. Stackhouse and R. Hagerman (1999). "Electrodermal responses to sensory stimuli in individuals with fragile X syndrome." Am J Med Genet**83**: 268-279.

Morales, J., L. Alonso-Nanclares, J.-R. Rodríguez, J. DeFelipe, Á. Rodríguez and Á. Merchán-Pérez (2011). "Espina: a tool for the automated segmentation and counting of synapses in large stacks of electron microscopy images." Frontiers in neuroanatomy**5**.

Musumeci, S., R. Hagerman, R. Ferri, P. Bosco, B. D. Bernardina, C. Tassinari, G. Sarro and M. Elia (1999). "Epilepsy and EEG findings in males with fragile X syndrome." Epilepsia**40**(8): 1092-1099.

Nicholson, D. A., R. Trana, Y. Katz, W. L. Kath, N. Spruston and Y. Geinisman (2006). "Distance-dependent differences in synapse number and AMPA receptor expression in hippocampal CA1 pyramidal neurons." Neuron**50**(3): 431-442.

Nimchinsky, E. A., A. M. Oberlander and K. Svoboda (2001). "Abnormal Development of Dendritic Spines inFMR1 Knock-Out Mice." The Journal of Neuroscience**21**(14): 5139-5146.

Okamoto, K.-I., T. Nagai, A. Miyawaki and Y. Hayashi (2004). "Rapid and persistent modulation of actin dynamics regulates postsynaptic reorganization underlying bidirectional plasticity." Nature neuroscience**7**(10): 1104-1112.

Osterweil, E. K., D. D. Krueger, K. Reinhold and M. F. Bear (2010). "Hypersensitivity to mGluR5 and ERK1/2 leads to excessive protein synthesis in the hippocampus of a mouse model of fragile X syndrome." The Journal of Neuroscience**30**(46): 15616-15627.

Palade, G. (1954). Electron microscope observations of interneuronal and neuromuscular synapses. Anatomical Record, WILEY-LISS DIV JOHN WILEY & SONS INC, 605 THIRD AVE, NEW YORK, NY 10158-0012.

Palay, S. (1957). "The morphology of synapses in the central nervous system." Experimental cell research**14**(Suppl 5): 275-293.

Palay, S. L. (1955). "Structure and function in the neuron." Progress in neurobiology**1**: 64-82.

Palay, S. L. (1956). "Synapses in the central nervous system." The Journal of biophysical and biochemical cytology**2**(4): 193-202.

Pan, F., G. M. Aldridge, W. T. Greenough and W.-B. Gan (2010). "Dendritic spine instability and insensitivity to modulation by sensory experience in a mouse model of fragile X syndrome." Proceedings of the National Academy of Sciences**107**(41): 17768-17773.

Park, J. S., M. C. Bateman and M. P. Goldberg (1996). "Rapid alterations in dendrite morphology during sublethal hypoxia or glutamate receptor activation." Neurobiology of disease**3**(3): 215-227.

Peters, A. (1987). Number of neurons and synapses in primary visual cortex. Cerebral cortex, Springer**:** 267-294.

Peters, A. and I. R. Kaiserman_Abramof (1970). "The small pyramidal neuron of the rat cerebral cortex. The perikaryon, dendrites and spines." American Journal of Anatomy**127**(4): 321-355.

Pooters, T., A. Van der Jeugd, Z. Callaerts-Vegh and R. D'Hooge (2015). "Telencephalic neurocircuitry and synaptic plasticity in rodent spatial learning and memory." Brain Research.

Popov, V., H. Davies, V. Rogachevsky, I. Patrushev, M. Errington, P. Gabbott, T. Bliss and M. Stewart (2004). "Remodelling of synaptic morphology but unchanged synaptic density during late phase long-term potentiation (LTP): a serial section electron

micrograph study in the dentate gyrus in the anaesthetised rat." Neuroscience**128**(2): 251-262.

Popov, V., N. Medvedev, I. Patrushev, D. Ignat'ev, E. Morenkov and M. Stewart (2007). "Reversible reduction in dendritic spines in CA1 of rat and ground squirrel subjected to hypothermia–normothermia in vivo: a three-dimensional electron microscope study." Neuroscience**149**(3): 549-560.

Portera-Cailliau, C. (2012). "Which comes first in fragile X syndrome, dendritic spine dysgenesis or defects in circuit plasticity?" The Neuroscientist**18**(1): 28-44.

Portera-Cailliau, C., D. T. Pan and R. Yuste (2003). "Activity-regulated dynamic behavior of early dendritic protrusions: evidence for different types of dendritic filopodia." The journal of neuroscience**23**(18): 7129-7142.

Purpura, D. P. (1974). "Dendritic spine" dysgenesis" and mental retardation." Science**186**(4169): 1126-1128.

Qin, M., J. Kang, T. V. Burlin, C. Jiang and C. B. Smith (2005). "Postadolescent changes in regional cerebral protein synthesis: an in vivo study in the FMR1 null mouse." The Journal of neuroscience**25**(20): 5087-5095.

Ramon y Cajal, S. (1893). "'New findings about the histological structure of the central nervous system." Archiv fur Anatomie und Physiologie (Anatomie)**17**: 319-428.

Restivo, L., F. Ferrari, E. Passino, C. Sgobio, J. Bock, B. A. Oostra, C. Bagni and M. Ammassari-Teule (2005). "Enriched environment promotes behavioral and morphological recovery in a mouse model for the fragile X syndrome." Proceedings of the National Academy of Sciences of the United States of America**102**(32): 11557-11562.

Retzius, G. (1891). Ueber den Bau der Oberflächenschicht der Grosshirnrinde beim Menschen und bei den Säugethieren, Aftonbladets Aktiebolags tryckeri.

Ronesi, J. A. and K. M. Huber (2008). "Metabotropic glutamate receptors and fragile x mental retardation protein: partners in translational regulation at the synapse." Science signaling**1**(5): pe6-pe6.

Rudelli, R., W. Brown, K. Wisniewski, E. Jenkins, M. Laure-Kamionowska, F. Connell and H. Wisniewski (1985). "Adult fragile X syndrome." Acta neuropathologica**67**(3-4): 289-295.

Schaffer, K. (1892). "Beitrag zur histologie der ammonshornformation." Archiv für Mikroskopische Anatomie**39**(1): 611-632.

Schubert, V. and C. G. Dotti (2007). "Transmitting on actin: synaptic control of dendritic architecture." Journal of cell science**120**(2): 205-212.

Segal, M. and E. Korkotian (2014). "Endoplasmic reticulum calcium stores in dendritic spines." Frontiers in neuroanatomy**8**.

Sheng, M. and C. C. Hoogenraad (2007). "The postsynaptic architecture of excitatory synapses: a more quantitative view." Annu. Rev. Biochem.**76**: 823-847.

Sherman, S., P. Jacobs, N. Morton, U. Froster-Iskenius, P. Howard-Peebles, K. Nielsen, M. Partington, G. Sutherland, G. Turner and M. Watson (1985). "Further segregation analysis of the fragile X syndrome with special reference to transmitting males." Human genetics**69**(4): 289-299.

Siomi, H., M. Choi, M. C. Siomi, R. L. Nussbaum and G. Dreyfuss (1994). "Essential role for KH domains in RNA binding: impaired RNA binding by a mutation in the KH domain of FMR1 that causes fragile X syndrome." Cell**77**(1): 33-39.

Song, F., P. Barton, V. Sleightholme, G. Yao and A. Fry-Smith (2003). "Screening for fragile X syndrome: a literature review and modelling study."

Sorra, K. E. and K. M. Harris (2000). "Overview on the structure, composition, function, development, and plasticity of hippocampal dendritic spines." Hippocampus**10**(5): 501-511.

Spacek, J. (1984). "Three-dimensional analysis of dendritic spines. II. Spine apparatus and other cytoplasmic components." Anatomy and embryology**171**(2): 235-243.

Spacek, J. and K. M. Harris (1997). "Three-dimensional organization of smooth endoplasmic reticulum in hippocampal CA1 dendrites and dendritic spines of the immature and mature rat." The Journal of neuroscience**17**(1): 190-203.

_pa_ek, J. and M. Hartmann (1983). "Three-Dimensional analysis of dendritic spines." Anatomy and Embryology**167**(2): 289-310.

Suetsugu, M. and P. Mehraein (1980). "Spine distribution along the apical dendrites of the pyramidal neurons in Down's syndrome." Acta neuropathologica**50**(3): 207-210.

Svoboda, K., D. W. Tank and W. Denk (1996). "Direct measurement of coupling between dendritic spines and shafts." SCIENCE-NEW YORK THEN WASHINGTON-: 716-718.

Tada, T. and M. Sheng (2006). "Molecular mechanisms of dendritic spine morphogenesis." Current opinion in neurobiology**16**(1): 95-101.

Tamanini, F., C. Bontekoe, C. E. Bakker, L. van Unen, B. Anar, R. Willemsen, M. Yoshida, H. Galjaard, B. A. Oostra and A. T. Hoogeveen (1999). "Different targets for the fragile X-related proteins revealed by their distinct nuclear localizations." Human molecular genetics**8**(5): 863-869.

Tao_Cheng, J. H., P. E. Gallant, M. W. Brightman, A. Dosemeci and T. S. Reese (2007). "Structural changes at synapses after delayed perfusion fixation in different regions of the mouse brain." Journal of Comparative Neurology**501**(5): 731-740.

Tonnesen, J., G. Katona, B. Rozsa and U. V. Nagerl (2014). "Spine neck plasticity regulates compartmentalization of synapses." Nat Neurosci**17**(5): 678-685.

Verkerk, A. J., M. Pieretti, J. S. Sutcliffe, Y.-H. Fu, D. P. Kuhl, A. Pizzuti, O. Reiner, S. Richards, M. F. Victoria and F. Zhang (1991). "Identification of a gene (FMR-1) containing a CGG repeat coincident with a breakpoint cluster region exhibiting length variation in fragile X syndrome." Cell**65**(5): 905-914.

Verkerk, A. J., M. Pieretti, J. S. Sutcliffe, Y. H. Fu, D. P. Kuhl, A. Pizzuti, O. Reiner, S. Richards, M. F. Victoria, F. P. Zhang and et al. (1991). "Identification of a gene (FMR-1) containing a CGG repeat coincident with a breakpoint cluster region exhibiting length variation in fragile X syndrome." Cell**65**(5): 905-914.

Warren, S. T. and D. E. H. c. M. Schalling (1993). "Tissue specific expression of FMR-1 provides evidence for a functional role in fragile X syndrome." Nature genetics**3**.

Weiler, I. J., S. A. Irwin, A. Y. Klintsova, C. M. Spencer, A. D. Brazelton, K. Miyashiro, T. A. Comery, B. Patel, J. Eberwine and W. T. Greenough (1997). "Fragile X mental retardation protein is translated near synapses in response to neurotransmitter activation." Proceedings of the National Academy of Sciences**94**(10): 5395-5400.

Wijetunge, L. S., J. Angibaud, A. Frick, P. C. Kind and U. V. Nägerl (2014). "Stimulated emission depletion (STED) microscopy reveals nanoscale defects in the developmental trajectory of dendritic spine morphogenesis in a mouse model of fragile X syndrome." The Journal of Neuroscience**34**(18): 6405-6412.

y Cajal, S. R. (1891). Sur la fine structure du lobe optique des oisseaux et sur l origine réelle des nerfs optiques.

Zalfa, F., B. Eleuteri, K. S. Dickson, V. Mercaldo, S. De Rubeis, A. Di Penta, E. Tabolacci, P. Chiurazzi, G. Neri and S. G. Grant (2007). "A new function for the fragile X mental retardation protein in regulation of PSD-95 mRNA stability." Nature neuroscience**10**(5): 578-587.

Zhou, Q., K. J. Homma and M.-m. Poo (2004). "Shrinkage of dendritic spines associated with long-term depression of hippocampal synapses." Neuron**44**(5): 749-757.

Appendix A: *Fmr1*

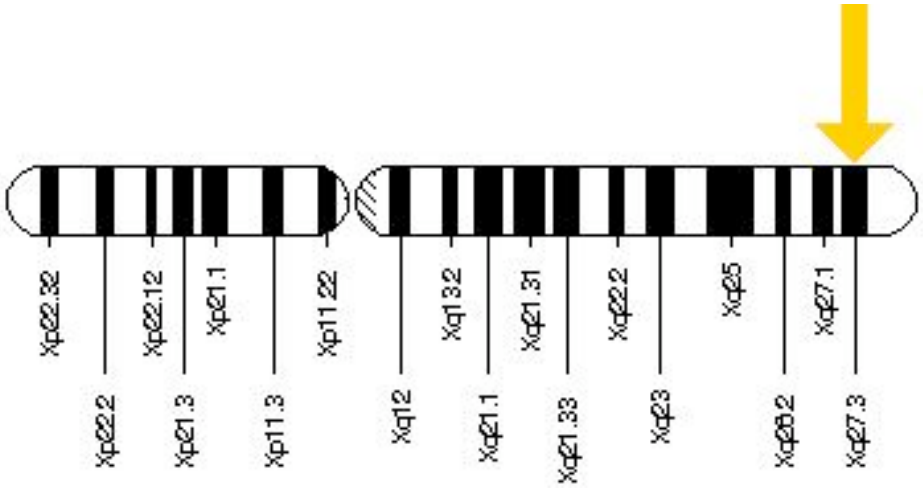

Figure 18:Cytogenetic location of *Fmr1*. The cytogenic location of *Fmr1* is Xq27.3. between base pairs 147,911,950 and 147,951,126 (Verkerk et al, 1991).

WT primers:

S1 = 5’ GTGGTTAGCTAAAGTGAGGATGAT 3’

S2 = 5’ CAGGTTTGTTGGGATTAACAGATC 3’

Primers used to amplify a fragment of 456 bp from the WT mouse allele

KO primers:

M2 = 5’ ATCTAGTCATGCTATGGATATCAGC 3’

N2= 5’ GTGGGCTCTATGGCTTCTGAGG 3’

Primers used to amplify a fragment of 800 basepairs from the *Fmr1*-/y mouse allele.

Appendix B: CA1 SR spine morphologies

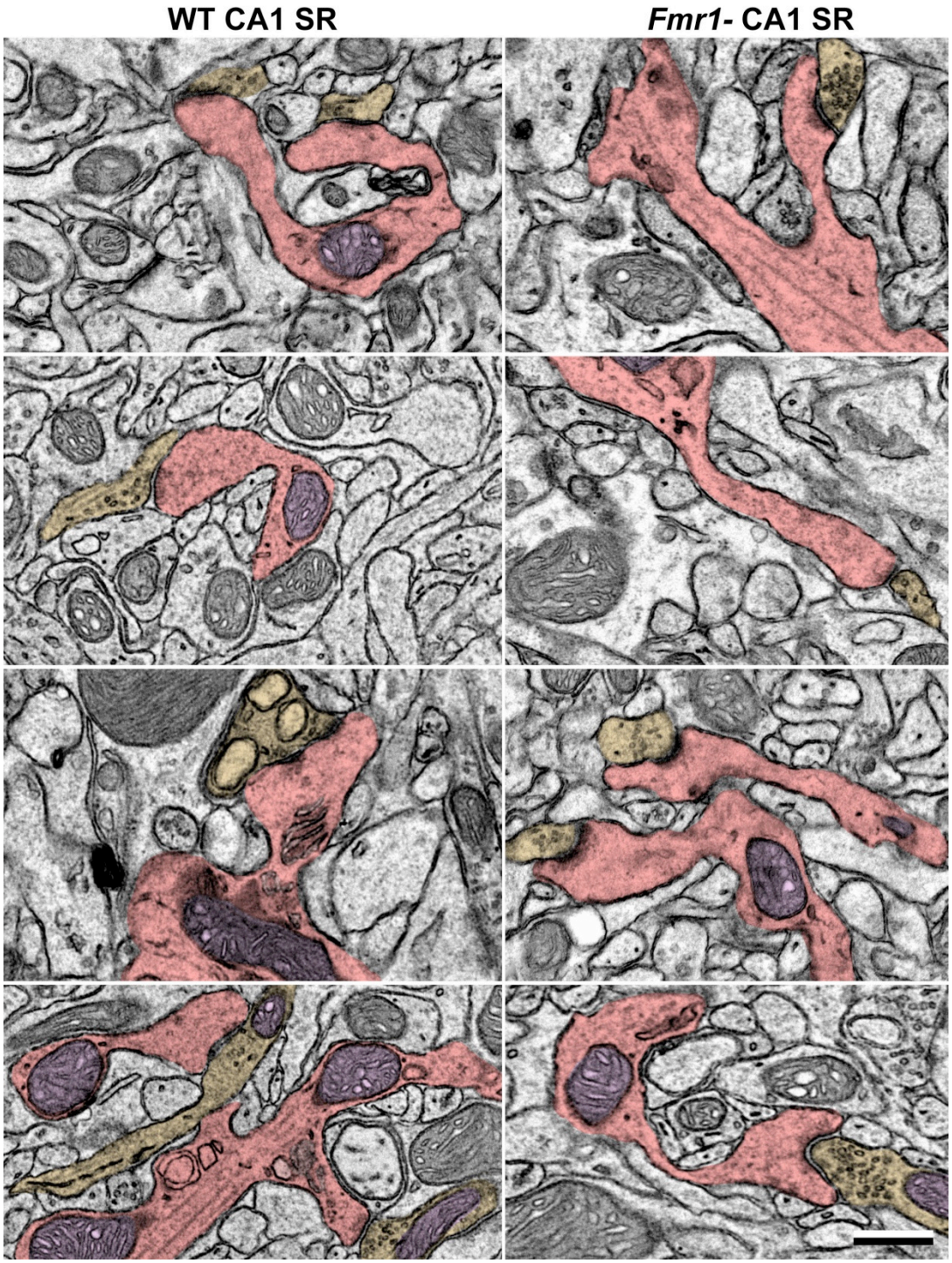

Figure 19: Dendritic spine morphologies from the CA1 SR. Examples of dendritic spines included in morphometric analyses. Scale bar = 500 nm.

Appendix C: DG MML spine morphologies

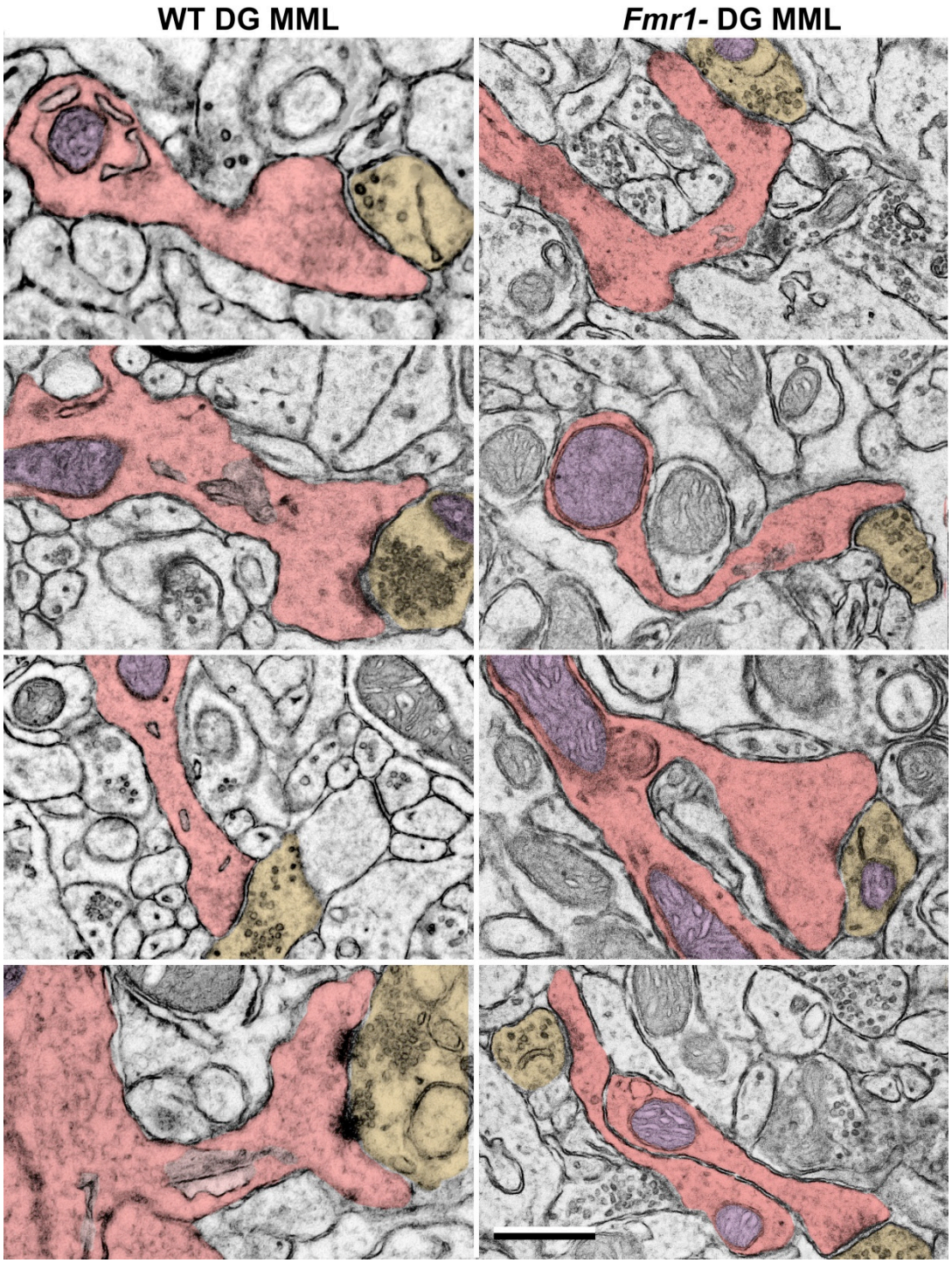

Figure 20: Dendritic spine morphologies from the DG MML. Examples of dendritic spines included in morphometric analyses. Scale bar = 500 nm.

Appendix D: Spine morphology scatterplots

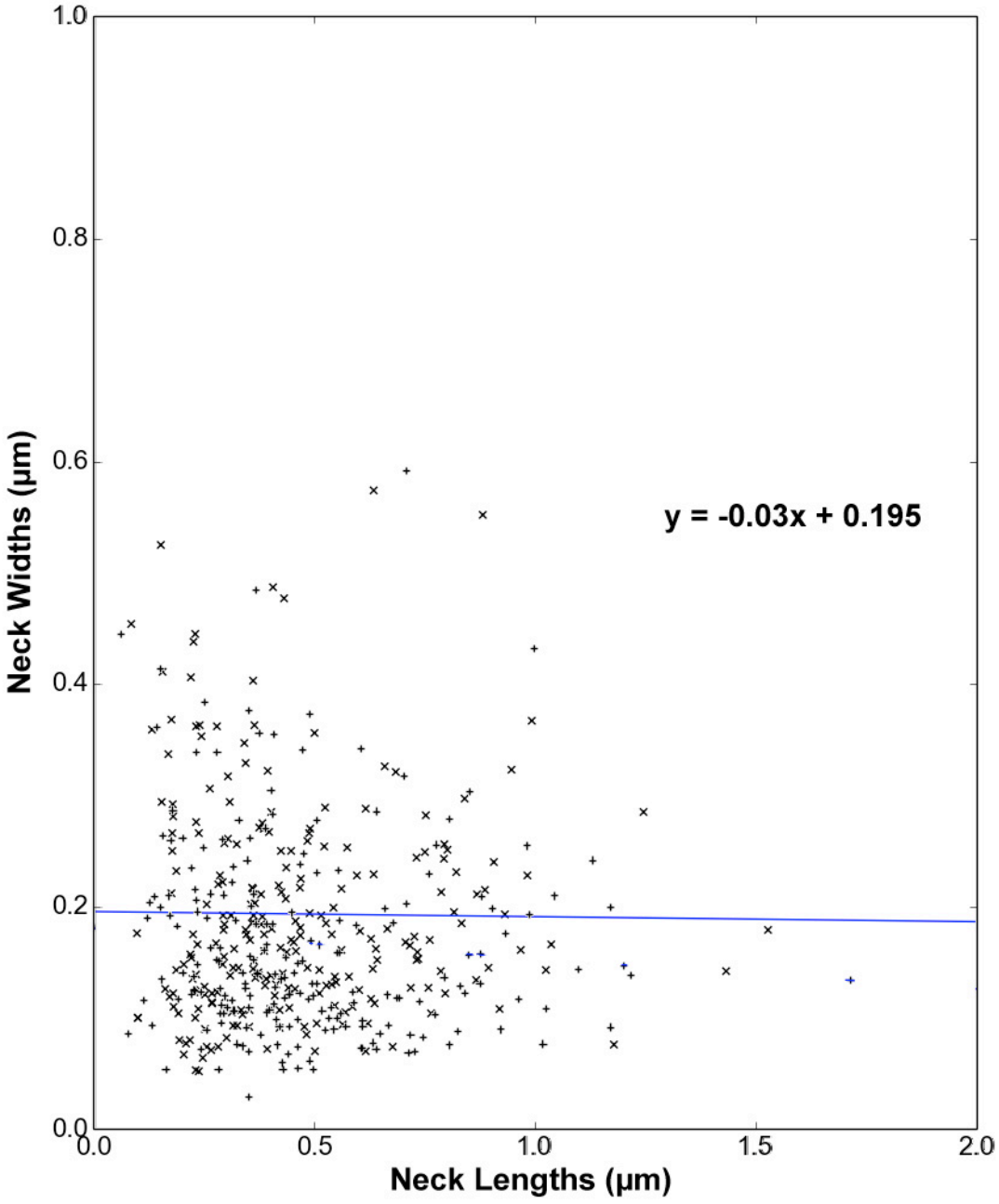

Figure 21: Comparison of spine neck widths and neck lengths. Scatterplot of all WT (x) and *Fmr1*- (+) neck widths and lengths from all spines used in morphological analyses. The relatively flat slope coefficient (-0.03) of the regression line (blue) indicates that there is not a significant correlation between spine neck widths and neck lengths.

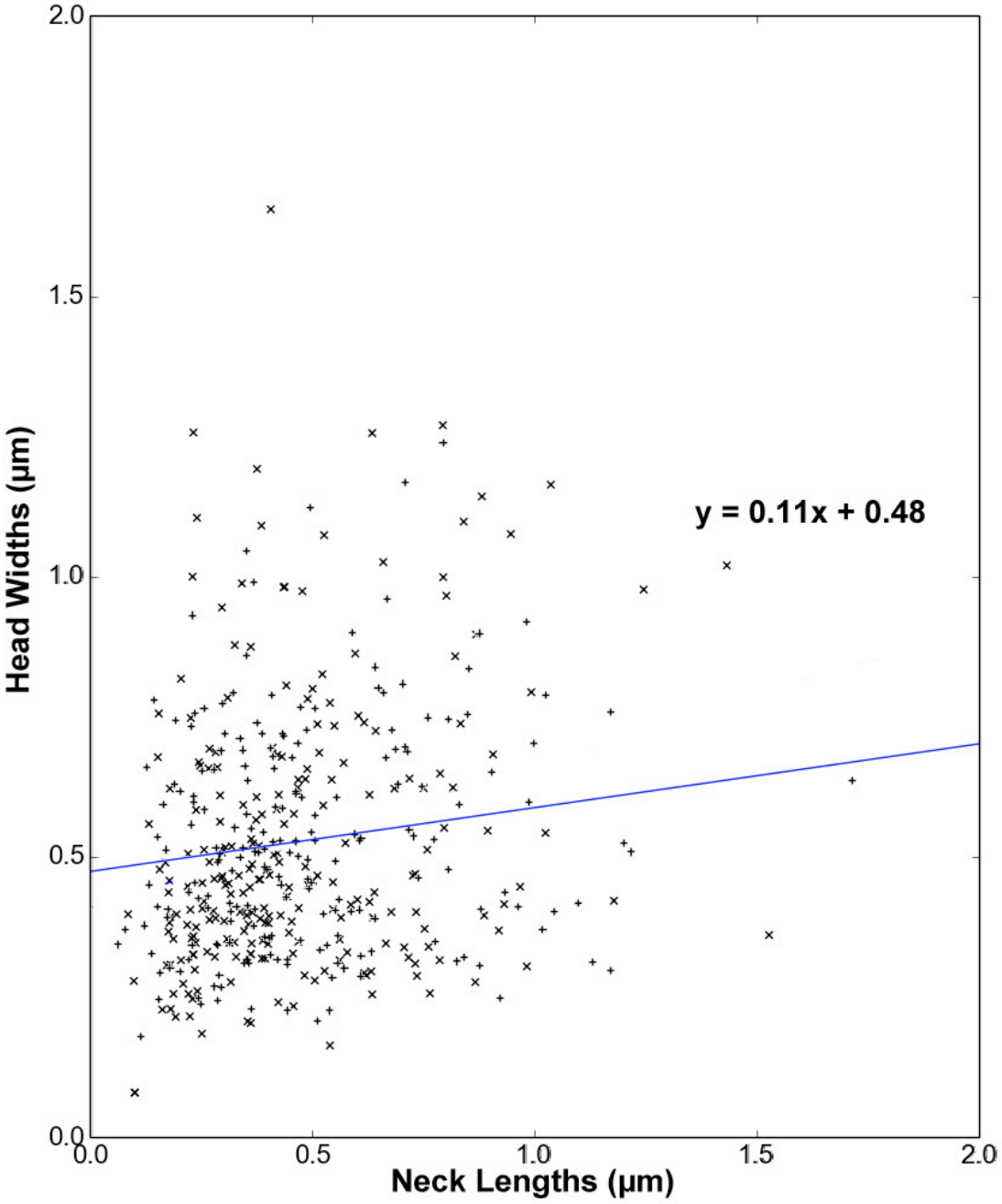

Figure 22: Comparison of spine head widths and neck lengths. Scatterplot of all WT (x) and *Fmr1*- (+) head widths and neck lengths from all spines used in morphological analyses The relatively flat slope coefficient (0.11) of the regression line (blue) indicates that there is not a significant correlation between spine head widths and neck widths.

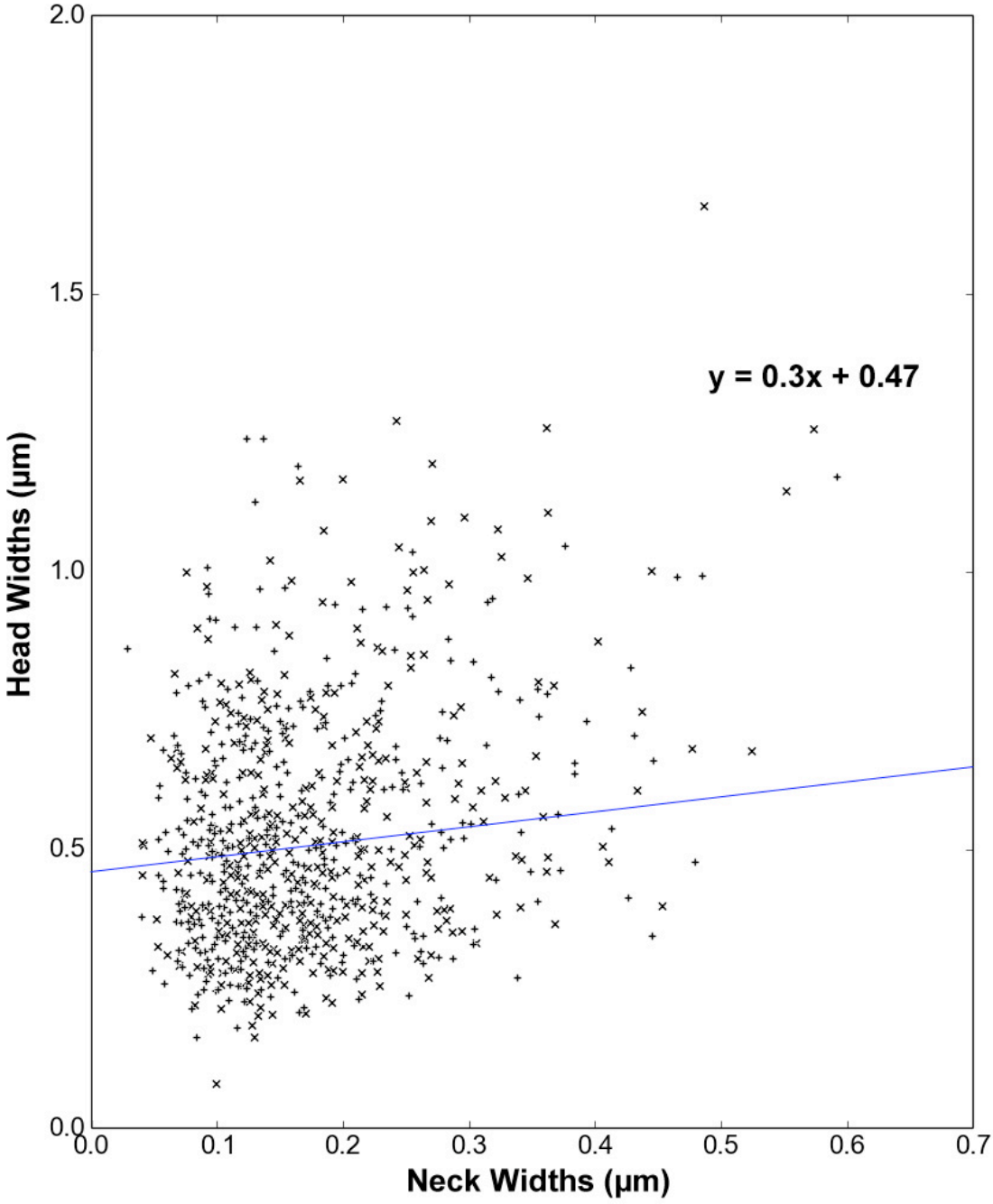
2.0
1.5
1.0
0.5
0.0
0.0
0.1
0.2
0.3
0.4
0.5
0.6
0.7
Head Widths (µm)
Neck Widths (µm)
y = 0.3x + 0.47

Figure 23: Comparison of spine head widths and neck widths. Scatterplot of all WT (x) and *Fmr1-* (+) head widths and neck widths from all spines used in morphological analyses. The relatively flat slope coefficient (0.3) of the regression analysis (blue line) indicates that spine head widths do not significantly correlate with neck widths. Furthermore, there is no clustering of points, which would indicate discrete categories of morphologies. These results indicate that, rather than discrete categories of spine morphologies (*i.e.,* mushroom, stubby, thin), dendritic spines in the CA1 and DG exhibit a continuum of morphologies.